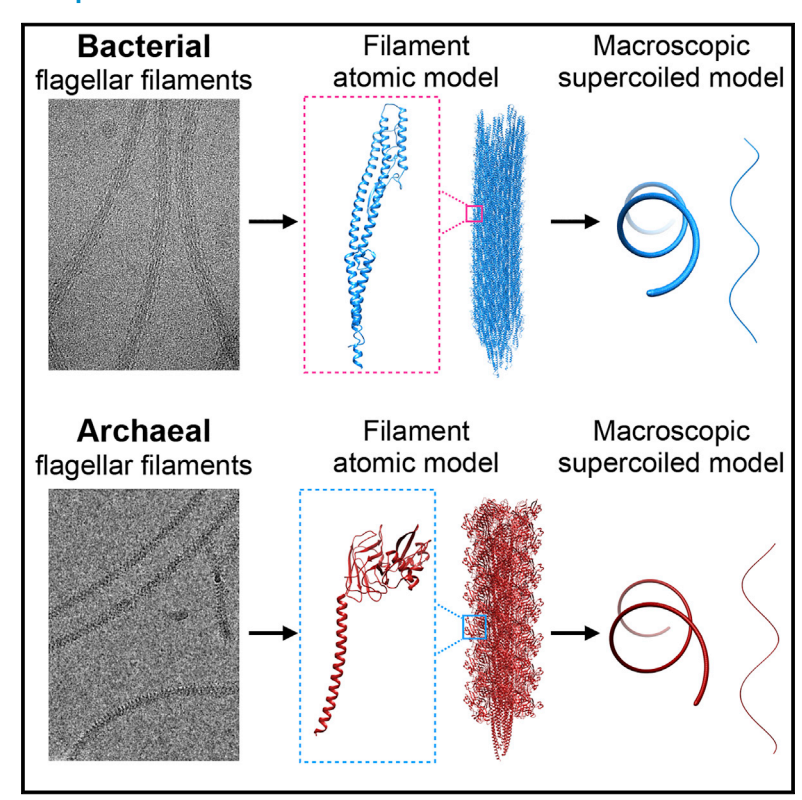


Convergent evolution in the supercoiling of prokaryotic flagellar filaments

Graphical abstract



Authors

Mark A.B. Kreutzberger, Ravi R. Sonani, Junfeng Liu, ..., Mart Krupovic, Birgit E. Scharf, Edward H. Egelman

Correspondence

egelman@virginia.edu

In brief

Although lacking homology between their structural components, archaeal and bacterial flagellar filaments achieve the supercoiling that powers locomotion through analogous mechanisms.

Highlights

- Cryo-EM can resolve the atomic structures of supercoiled flagellar filaments
- Supercoiled atomic structures show 11 states in bacteria and 10 states in archaea
- Distinctly different structures have evolved to form similar supercoils





Cell



Article

Convergent evolution in the supercoiling of prokaryotic flagellar filaments

Mark A.B. Kreutzberger, ¹ Ravi R. Sonani, ¹ Junfeng Liu, ² Sharanya Chatterjee, ³ Fengbin Wang, ¹ Amanda L. Sebastian, ⁴ Priyanka Biswas, ³ Cheryl Ewing, ⁵ Weili Zheng, ¹ Frédéric Poly, ⁵ Gad Frankel, ³ B.F. Luisi, ⁶ Chris R. Calladine, ⁷ Mart Krupovic, ² Birgit E. Scharf, ⁴ and Edward H. Egelman^{1,8,*}

SUMMARY

The supercoiling of bacterial and archaeal flagellar filaments is required for motility. Archaeal flagellar filaments have no homology to their bacterial counterparts and are instead homologs of bacterial type IV pili. How these prokaryotic flagellar filaments, each composed of thousands of copies of identical subunits, can form stable supercoils under torsional stress is a fascinating puzzle for which structural insights have been elusive. Advances in cryoelectron microscopy (cryo-EM) make it now possible to directly visualize the basis for supercoiling, and here, we show the atomic structures of supercoiled bacterial and archaeal flagellar filaments. For the bacterial flagellar filament, we identify 11 distinct protofilament conformations with three broad classes of inter-protomer interface. For the archaeal flagellar filament, 10 protofilaments form a supercoil geometry supported by 10 distinct conformations, with one inter-protomer discontinuity creating a seam inside of the curve. Our results suggest that convergent evolution has yielded stable superhelical geometries that enable microbial locomotion.

INTRODUCTION

Many organisms from the three domains of life, Archaea, Bacteria, and Eukarya, possess flagella, which allow for motility (Khan and Scholey, 2018). In an example of convergent evolution, these three systems evolved independently with entirely different components yet similar functions. Eukaryotic flagella are composed of microtubules, and ATP hydrolysis by dynein motors causes the appendages to beat back and forth (Khan and Scholey, 2018). Bacterial and archaeal flagella convey motility through the motor-driven rotation of supercoiled flagellar filaments that function as propellers (Nedeljković et al., 2021; Poweleit et al., 2016). Although the eukaryotic flagella and cilia are quite complex with as many as 600 different proteins (Pazour et al., 2005), bacterial and archaeal flagellar filaments (AFFs) are both polymerized from a single kind of subunit, flagellin.

The bacterial flagellum has been studied extensively (Macnab, 2003; Nedeljković et al., 2021), and the supercoiling of its flagellar filament and its polymorphic ability to switch between waveforms during the alternation of swimming modes are indispensable for motility (Darnton et al., 2007). When bacteria such

as Escherichia coli (E. coli) and Salmonella typhimurium switch from running to a tumble, one or multiple flagellar filaments break out of a bundle due to the change in the direction of motor rotation. This change in mechanical force causes the waveforms of the flagellar filament to switch from being normal waveforms in the bundle to being either or both of the semi-coiled and curly I waveforms (Darnton et al., 2007). These semi-coiled and curly I waveforms are more favorable than the normal waveforms after the change from counterclockwise (CCW) to clockwise (CW) rotation. The various polymorphisms of the bacterial flagellar filament (BFF) differ from each other in both the pitch and curvature of the supercoil and can be distinguished using light or electron microscopy.

For the BFF, the core domains D0 and D1 are crucial to supercoiling and polymorphism (Kanto et al., 1991; Yoshioka et al., 1995), whereas the outer domains can have diverse structures or be largely absent (Kamiya et al., 1982; Kreutzberger et al., 2022; Trachtenberg and DeRosier, 1988). Almost all structural studies of the BFF have been performed using straight non-motile flagellar filaments produced by point mutations in the flagellin subunit (Maki-Yonekura et al., 2010; O'Brien and Bennett,



¹Department of Biochemistry and Molecular Genetics, University of Virginia School of Medicine, Charlottesville, VA 22903, USA

²Institut Pasteur, Université Paris Cité, CNRS UMR 6047, Archaeal Virology Unit, 75015 Paris, France

³Centre for Molecular Microbiology and Infection, Department of Life Sciences, Imperial College London, London, UK

⁴Department of Biological Sciences, Virginia Tech, Blacksburg, VA 24061, USA

⁵Enteric Diseases Department, Naval Medical Research Center, Silver Spring, MD 20910, USA

⁶Department of Biochemistry, University of Cambridge, Tennis Court Road, Cambridge CB2 1GA, UK

⁷Department of Engineering, University of Cambridge, Trumpington Street, Cambridge CB2 1PZ, UK

⁸Lead contact

^{*}Correspondence: egelman@virginia.edu https://doi.org/10.1016/j.cell.2022.08.009



1972; Trachtenberg and DeRosier, 1988; Wang et al., 2017; Yamashita et al., 1998; Yonekura et al., 2003). These point mutations lock the BFF into structures in which 11 protofilaments have either all left-handed (L-type) or all right-handed (R-type) configurations (Hyman and Trachtenberg, 1991), with the filament subunits related by strict helical symmetry. These straight filaments were used for structural studies, as it was believed, until recently (Blum et al., 2019; Kreutzberger et al., 2022; Montemayor et al., 2021), that high-resolution structural studies of supercoiled filaments were unobtainable. The observation of only two structural states coupled with flagellin polymerization studies (Asakura, 1970) resulted in the development of a two-state model for the supercoiling of the BFF (Calladine, 1975; Calladine et al., 2013; Calldine, 1978). The "2-state model" (Maki-Yonekura et al., 2010) referred to the idea that the protofilaments existed in one of two discrete states and that the interface between those differing protofilaments (along the 11-start cylindrical surface lattice lines) is a "2-way (allosteric) switch."

Here, we present near-atomic resolution cryo-EM structures of three supercoiled BFFs in one of two waveforms from two different strains of *E. coli*, Enteropathogenic *E. coli* O127:H6 (EPEC H6) and *E. coli* K-12. We focused on only the core domain structures of these filaments, as those are key to supercoiling. We show that there are 11 protofilament states in both the normal- and curly-l-waveform structures, which is similar to the recent results obtained for the flagellar hook (Kato et al., 2019; Shibata et al., 2019). The interfaces between those differing protofilaments cluster into distinct groups, consistent with allosteric switching.

Although the bacterial flagellum has been extensively studied, much of the work on the archaeal system is more recent (Bardy et al., 2002; Gambelli et al., 2022; Ghosh and Albers, 2011; Khan and Scholey, 2018; Poweleit et al., 2016). The AFF and archaeal flagellin have no homology to their bacterial analogs and are instead related to bacterial and archaeal type IV pili (T4P) (Bayley and Jarrell, 1998; Cohen-Krausz and Trachtenberg, 2002; Ortega and Beeby, 2021; Thomas et al., 2001). Despite their similarities, AFFs must be able to supercoil (Bardy et al., 2002), whereas T4P do not. Recently, it was suggested that the flexibility of the AFF allowed for motility (Gambelli et al., 2022), but this hypothesis is unlikely because the rotation of a flexible filament would not produce thrust. However, no structural models for the supercoiling of AFFs have been proposed.

We also report the cryo-EM structure of the supercoiled AFF from the thermoacidophilic *Saccharolobus islandicus* REY15A and show that it is assembled by 10 protofilaments, each in a different conformation. Here, supercoiling is governed by a core domain, containing a single α -helix in archaea rather than the coiled-coils in bacterial filaments. In contrast to the bacterial filaments, a discrete seam exists between protofilaments on the inside of the archaeal supercoil.

RESULTS

Cryo-EM structures of supercoiled bacterial flagellar filaments

We used cryo-EM to determine the structure of supercoiled BFFs from EPEC O127:H6 (H6) and *E. coli* K-12 (K-12) (Figures 1

and S1). For this work, we focused on the core domains D0 and D1 and masked out the outer domains from the H6 flagellar filament reconstruction. Although we have previously shown that the outer domains in H6 form tetramers (that are dimers of dimers) (Kreutzberger et al., 2022), the pairings of the outer domains do not introduce any observable perturbation of the core domains D0 and D1. The H6 flagellar filaments were imaged under two different buffer conditions, which results in different curvatures and supercoil pitches (Figures 1, S1A, S1D, and S1G).

We initially performed a helical reconstruction, refining a single global helical symmetry relating all subunits to each other (Figure S1). In all cases, we were able to reconstruct the flagellar core domains D0 and D1 to ~4.0 Å resolution. For each helical structure, the "gold-standard" Fourier shell correlation (FSC) (GS FSC) appeared to over-estimate the map resolution (Figures S1C, S1F, and S1I; Table S1), most likely due to the fact that the GS FSC is a measure of reproducibility and not of true resolution, particularly for structures with imposed symmetry (Subramaniam et al., 2016). The average protofilament tilt for the various bacterial flagellar waveforms has previously been predicted from the number of L- and R-protofilaments expected to be present in the structure (Calladine et al., 2013). The higher curvature H6 BFFs (Figures 1B and S1A) appear to be in the curly I waveform due to the tilt and rise of +0.94°/52.9 Å for subunits along a protofilament in the helical reconstruction, which can be easily seen in the helical net representation of the symmetry (dashed lines in Figure S1B). The lower curvature H6 and K-12 flagellar filaments appear to be in the normal waveform with a protofilament tilt and rise of $-0.6^{\circ}/53.1$ Å (Figures S1E and S1H).

We developed a scheme (Figure 1A) for determining the structure of supercoiled flagellar filaments using cryo-EM, starting with helical reconstruction and then employing a low-pass filtered version of that reconstruction as the starting point for an asymmetric reconstruction using the various tools in cry-SPARC (Puniani et al., 2017). We solved the higher curvature EPEC H6 structure to 3.4 Å resolution, whereas the lower curvature EPEC H6 and the E. coli K12 BFF structures were solved to 4.2 and 3.5 Å resolution, respectively. Given that the starting volumes had been low-pass filtered to 20-50 Å, there was no possibility that the details in the final asymmetric reconstructions were biased by the initial models. The resolution of each of these BFFs varied locally between the subunits on the inner and outer curves (Figures S2A-S2F). Based on both the helical symmetry parameters (Calladine et al., 2013) as well as the 2.9-rad/μm curvature estimated from our map (Table S2), we are confident that the this higher curvature H6 structure (Figures 1B-1D and S2A) is in the curly I waveform. Likewise, based on the average protofilament tilt and curvature of \sim 1–1.4 rad/ μ m (Table S2), the lower curvature H6 and K-12 structures (Figures 1E-1G, and S2C, and S2E) are in the normal waveform.

We compared the subunit density map from our EPEC H6 curly I helical and asymmetric reconstructions with the nominal $2.8\,\text{Å}$ resolution helically symmetric structure from the Firmicutes *Kurthia* (Blum et al., 2019). The H6 curly I helical reconstruction had a GS FSC resolution estimate of $2.9\,\text{Å}$. However, using the d_{99} and d_{model} resolution estimates (Afonine et al., 2018a), we estimated $3.5\,\text{and}~3.2\,\text{Å}$ resolution, respectively, for the *Kurthia*



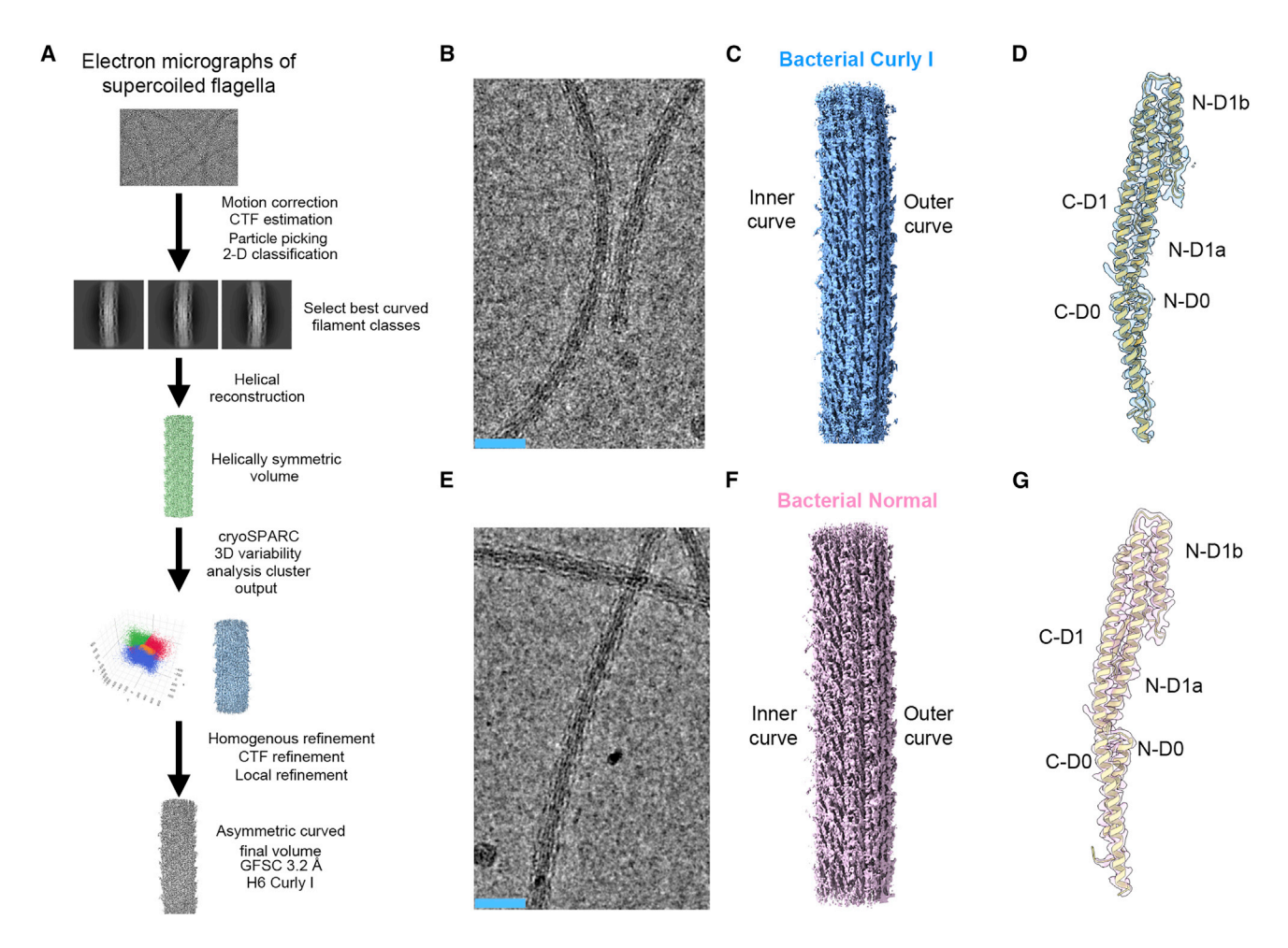


Figure 1. Cryo-EM structures of the bacterial flagellar filament core in the curly I and normal waveforms

- (A) The general scheme used for the asymmetric reconstruction of supercoiled flagellar filaments.
- (B) Cryo-electron micrograph of the H6 flagellar filaments with a high degree of curvature. The scale bar is ~30 nm.
- (C) Cryo-EM reconstruction of the H6 flagellar filament in the curly-I-waveform state.
- (D) The 3.4 Å density map of a single curly I subunit (light blue) with a model built in (gold).
- (E) Cryo-electron micrograph of the EPEC H6 flagellar filaments with less curvature. The scale bar is ∼30 nm.
- (F) The 3.9 Å cryo-EM reconstruction of the H6 flagellar core in the normal-waveform state.
- (G) The 3.2 Å density map of the core domains for a single K-12 flagellin in the normal-waveform state. See also Figures S1 and S2.

filament as well as 3.5 and 3.4 Å, respectively, for the H6 curly I. This highlights the notion that the map:map FSC is more a metric of reproducibility rather than true resolution (Subramaniam et al., 2016). Both the Kurthia and H6 helical structures' density maps had discontinuous density in the loop region connecting the two helices of N-terminal domain D1 (Figures S2G and S2H). The flagellin subunit densities in the asymmetric curly I structure did not have broken density in this loop (Figure S2I) and yielded a higher quality map despite having a lower resolution estimated by the "gold-standard" 0.143 map:map FSC. We built models into our flagellar filament structures (Figures 1D and 1G) and used the more conservative map:model FSC threshold of 0.5 for the resolution estimate. We found a similar improvement in map quality when we analyzed the normal-waveform asymmetric reconstructions from H6 and K-12, which had resolution estimates of 4.2 and 3.5 Å, respectively (Figures S2C and S2E).

Modeling the supercoiling of flagellar filaments

Because the diameter of supercoiled waveforms (~2,000-6,000 Å) is significantly larger than the typical ice thickness in a cryo-EM grid (Rice et al., 2018), we suspected that the supercoiling of the flagellar filaments would be constrained in the z dimension. Cryo-electron tomography on wild-type Campylobacter jejuni flagellar filaments (Figures S3A-S3D) indeed showed that the flagellar filaments were mostly flattened in the z dimension (Figure S3D). It has previously been suggested that BFFs that are flattened by negative-stain TEM preparative conditions retain their local curvature and undergo a large twist at select locations to accommodate the flattening without severe distortions elsewhere (Calldine, 1978). We anticipated that the very small segments of flagella in our particles (\sim 0.04–0.07 μ m) relative to the overall length of the flagellar filament (2-10 µm) could also be undistorted for the same reasons. To test this, we developed a



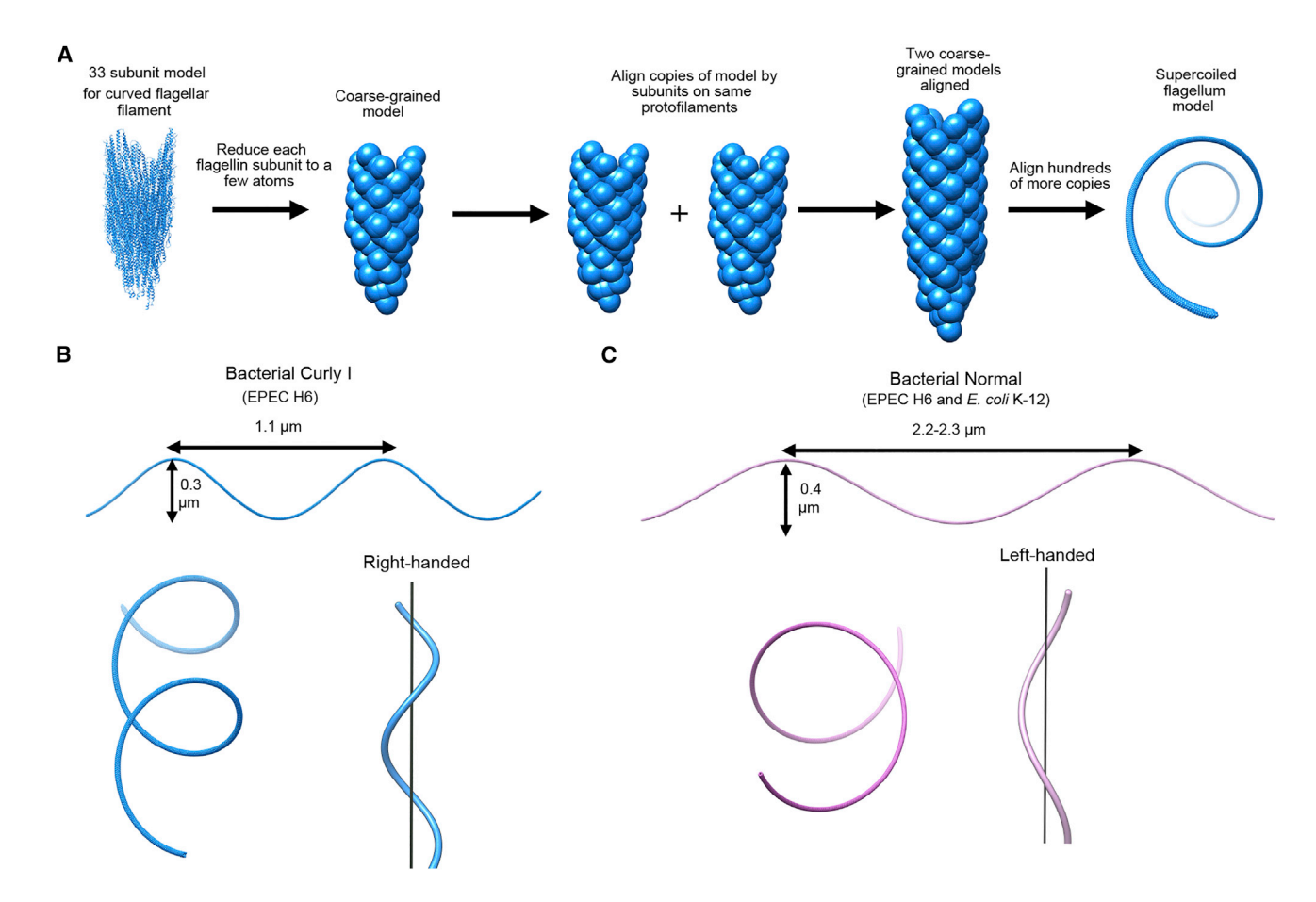


Figure 2. Supercoiled model of the bacterial flagellar filament

(A) Scheme for modeling the three-dimensional supercoil of prokaryotic flagellar filaments, starting from an atomic model built from cryo-EM data.

(B) The supercoiled model of the curly I waveform of the bacterial flagellar filament. The top image shows the "side view of the filament," where the supercoil pitch and diameter are easily seen. The bottom left image shows a view "through" the supercoil. The bottom right image shows the right handedness of the curly I waveform, with the helical axis of the supercoil being represented by the black line.

(C) Supercoiled model of the normal bacterial flagellar waveform. The H6 model had a pitch of 2.3 μm and a diameter of 0.4 μm. The K-12 model had a pitch of 2.2 μm and a diameter of 0.4 μm. The left hand of the normal supercoil is shown in the bottom right image. See also Figure S3.

method for aligning hundreds of copies of flagellar filament atomic models to generate a macroscopic model (Figure 2A). Using this scheme, the supercoil for the curly I waveform (Figure 2B) had a pitch of 1.1 μm and a diameter of 0.3 μm (Kamiya and Asakura, 1976; Turner et al., 2000) from the atomic model. These parameters and the waveform's right handedness are consistent with the literature (Turner et al., 2000). We obtained a similar result for modeling the supercoil of the normal structures (Figure 2C). For H6, the pitch was 2.3 µm and diameter was 0.4 μm. The K-12 supercoiled model produced a similar result, where the pitch was 2.2 μm and the diameter was 0.4 µm. Both of the normal supercoils were left handed, and the parameters agreed well with the literature (Table S1) (Kamiya and Asakura, 1976; Turner et al., 2000). Thus, despite the flattening of the overall supercoil in ice, the flagellar filaments retained the local curvature and twist of a flagellum supercoiling in three dimensions. Thus, the microscopic, short-curved BFF structures were indeed representative of the macroscopic supercoiled state, which has continuous uniform curvature in three dimensions.

Supercoiling of the bacterial flagellar filament is created by 11 flagellin conformations

When assessing the flagellin conformations, we used subunits on the inner and outermost regions of the curve as references (Figure 3A). For both, curly I and normal structures, the innercurve subunits were shorter than the outer curve ones when aligned by domain D0 (Figures 3B and 3C). We next aligned subunits from each of the 11 protofilaments by domain D1, and we identified 11 flagellin conformations for each waveform state (Figures 3D and 3E). The 11 conformations of curly I flagellins (Figure 3D) were more different from each other than those of the normal (Figure 3E). Importantly, we found that subunits from the same protofilament had nearly identical conformations when aligned by domain D0 compared with subunits from adjacent protofilaments (Figure S3E–S3H). We concluded that the



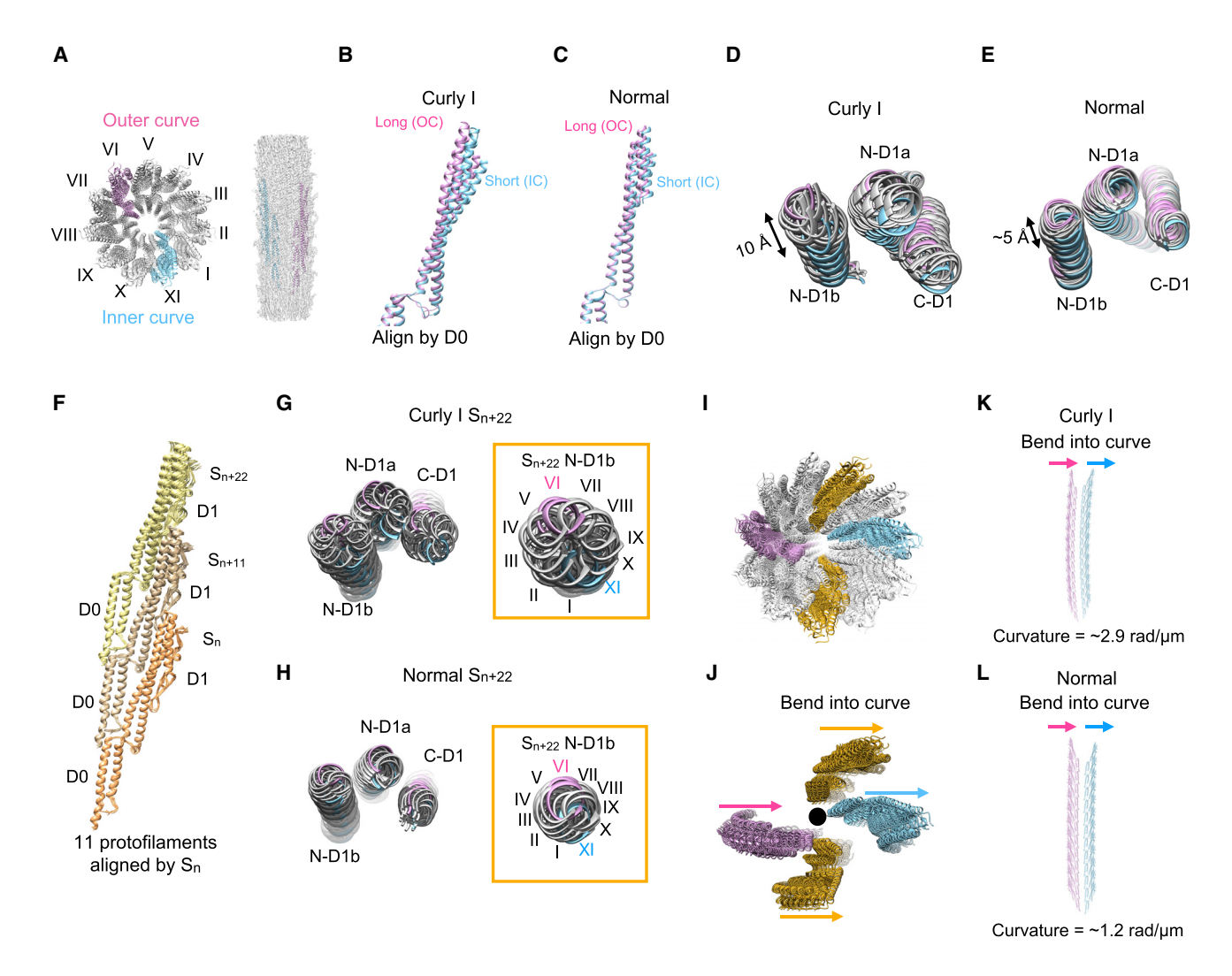


Figure 3. Subunit and protofilament states in the bacterial flagellar filament

- (A) Top and side views of the flagellar core model (left) and map (right) with inner and outer protofilaments colored blue and pink, respectively.
- (B) Alignment of two curly I flagellins from the inner (blue) and outer (pink) curve protofilaments.
- (C) Alignment of two normal flagellins.
- (D) Alignment of curly I flagellin subunits from each protofilament by domain D0. The double arrow represents the end-to-end distance between an inner curve protofilament (light blue) and an outer curve protofilament (pink).
- (E) Alignment of normal flagellin subunits from each protofilament by domain D0.
- (F) Alignment of each of the 11 curly I protofilaments by subunit S_n.
- (G) View of subunit S_{n+22} of each of the 11 curly I protofilaments that have been aligned by subunit S_n. The orange inset shows a close-up view of domain N-D1b of Sn+22 from this alignment. The pink and blue protofilaments correspond to protofilaments in the outer and inner curves, respectively.
- (H) View of subunit S_{n+22} of each of the 11 normal-waveform (K-12) protofilaments.
- (I) Top-down view of the curly I filament model shows the inner (blue) and outer (pink) curve protofilaments as well as protofilaments in between the inner- and outermost regions of the curve (gold).
- (J) Same view as in (I) but with only the colored protofilaments shown. The arrows indicate the direction in which the protofilaments bend.
- (K) Side view of the inner (light blue) and outer (pink) curly I protofilaments.
- (L) Side view of the inner (light blue) and outer (pink) normal protofilaments.

See also Figure S3.

small differences between subunits on the same protofilament are caused by noise and/or modeling error (Figures S3I-S3L).

We then compared the protofilaments of curly I and normal waveforms by aligning each of the individual 11 protofilaments by the first subunit (S_n) of each protofilament model (Figure 3F).

From this alignment, we identified 11 protofilament states by examining the top view of subunit S_{n+22} from each protofilament. Differences between each of the curly I protofilaments (Figure 3G) were greater than those of the normal (Figure 3H). Nevertheless, the protofilaments in both waveforms differed from





each other according to the same circular pattern (Figures 3G and 3H) where adjacent protofilaments were more similar to each other than non-adjacent ones. This pattern can be more easily explained by considering their position in the supercoiled structure (Figures 3I and 3J). The same amino acid residues face the center of the lumen in each structure. However, the tilt of each protofilament with respect to the center of the flagellar filament is different. Each of the protofilaments is bending into the curve (Figure 3J). The innermost protofilament (blue) in the curve is tilting away from the central axis of the filament. The outermost protofilament (pink) is tilting toward the central axis, and the protofilaments intermediate between the outer and inner curves (gold) are tilting in a plane skew to the filament's central axis. The extent of protofilament bending into the curve is greater in the curly I (Figure 3K) state than in the normal form (Figure 3L), consistent with the greater curvature in the former.

The 5-start interfacial switch of supercoiled bacterial flagellar filaments

Historically, the switching between L and R states was viewed to occur along the 5-start interface (Figures 4A and 4B) (Calladine et al., 2013). This 5-start interface constitutes the interface between adjacent protofilaments, whereas the 11-start interface is the interface between two subunits in the same protofilament. For the curly I structure, we find three classes of 5-start interfaces (Figures 4C-4E), with 5 longer outer curve interfaces (red, Figures 4C-4E), four shorter inner curve interfaces (blue, Figures 4C-4E), and two interfaces of intermediate height (purple, Figures 4C-4E) in between the inner and outer curve protofilaments. For the normal structures, we observed a similar pattern except that the intermediate interfaces did not exist (Figures 4F-4H, S4A and S4B). Instead, there were three shorter protofilaments (indigo, Figures 4F-4H) and eight longer ones (red, Figures 4F-4H) with less of a height difference between the inner and outer interfaces in the normal compared with the curly I. These classes of protofilament height were also only in the z dimension, and a continuous distribution of protofilament conformations was present in the x and y dimensions (Figures 4D and 4G).

Because wild-type filaments do not naturally exist in the all-L or all-R states, supercoiling might be a consequence of the kinetic trapping that keeps these filaments away from these minimum energy states. We performed a simple annealing experiment by heating supercoiled flagellar filaments from room temperature to 55°C and allowing them to slowly cool to room temperature (Figures S4C and S4E). The BFFs retained their supercoil (Figures S4D and S4F), suggesting that the supercoiled state is a favorable energy state under our experimental conditions.

Cryo-EM structure of the supercoiled archaeal flagellar filament

We next sought to apply our method for reconstructing supercoiled flagellar filaments to AFFs from *S. islandicus* REY15A. Electron micrographs revealed two distinct filament populations (Figures 5A and 5B). These were either supercoiled and identified as AFFs or not supercoiled and identified as archaeal T4P. Differences in the surface structures of flagellar filaments and T4P were also observed in cryo-EM images (Figure 5B). Using the same workflow as the one used for the BFF reconstruction, we solved the structure of the REY15A flagellar filament imposing a global helical symmetry, which resulted in a density map at \sim 4 Å resolution (Figure S5A). We then reconstructed the REY15A flagellar filament asymmetrically and obtained a 3.4 Å resolution map with clear curvature (Figures 5C and S5B) and modeled the flagellin subunits into the map (Figures 5D and 5F). From this short asymmetric reconstruction, we estimated the curvature to be \sim 2 radians/ μ m (Table S2). Similar to many AFFs and T4P (Gambelli et al., 2022; Poweleit et al., 2016; Wang et al., 2020; Wang et al., 2019), we detected extensive glycosylation with several N-linked glycans on the surface of the structure (Figures 5D and 5E). We also found an indication of tyrosine glycosylation (Figures S5F and S5G), which is uncommon but has been previously observed in prokaryotes (Zarschler et al., 2010).

The N-terminal regions of the preprocessed forms of archaeal flagellins and bacterial and archaeal type IV pilins exist as transmembrane domains (Thomas et al., 2001). After cleavage, these mature subunits assemble into their respective polymers in the absence of a membrane. Interestingly, TMHMM (Sonnhammer et al., 1998) analysis of transmembrane regions for the REY15A flagellin predicted additional transmembrane regions in the C-terminal outer domain (Figure 6A). These regions are either β-sheets or loops in the flagellar filament structure (Figure S6B). We took the sequences for each of the predicted C-terminal transmembrane regions and analyzed their structure using AlphaFold (Jumper et al., 2021). For both of the ~20 amino acid residue spanning regions, the predicted models were α -helical (Figures S6C and S6D). As a control, a region predicted not to be transmembrane and that was part of a β -sheet in the filament was predicted to be a β-hairpin by AlphaFold2 (Figure S6E). We speculate that these regions of the C-terminal outer domain are indeed transmembrane helices in the preprocessed flagellin monomers and inserted in the archaeal membrane prior to assembly.

The supercoiled archaeal flagellar filament is assembled from 10 protofilaments

The S. islandicus REY15A genome (Makarova et al., 2016) only encodes a single flagellin, unlike some other species of archaea (Gambelli et al., 2022), which simplifies the interpretation of our results. For example, it is now clear that multiple flagellins within the same filament are not needed for supercoiling. In addition to a prominent 3-start helix with extensive glycosylation (Figures S6F and S6G), the REY15A flagellar filament also has a less prominent 10-start surface helix. When comparing helical nets (Figures 6H and 6I), the 10-start helices in archaea (Figures S6I and S6J) are reminiscent of the nearly vertical 11-start protofilaments of the BFFs because both filaments have low twist (Figures S6H and S6I). The 10-start interactions mainly occur for the N-terminal α -helical domain at a relatively small radius in the filament. When we aligned a single subunit from each of these strands, there were 10 subunit states with one of these states being markedly different from any of the others (Figure 5E). We also found that the subunits on the



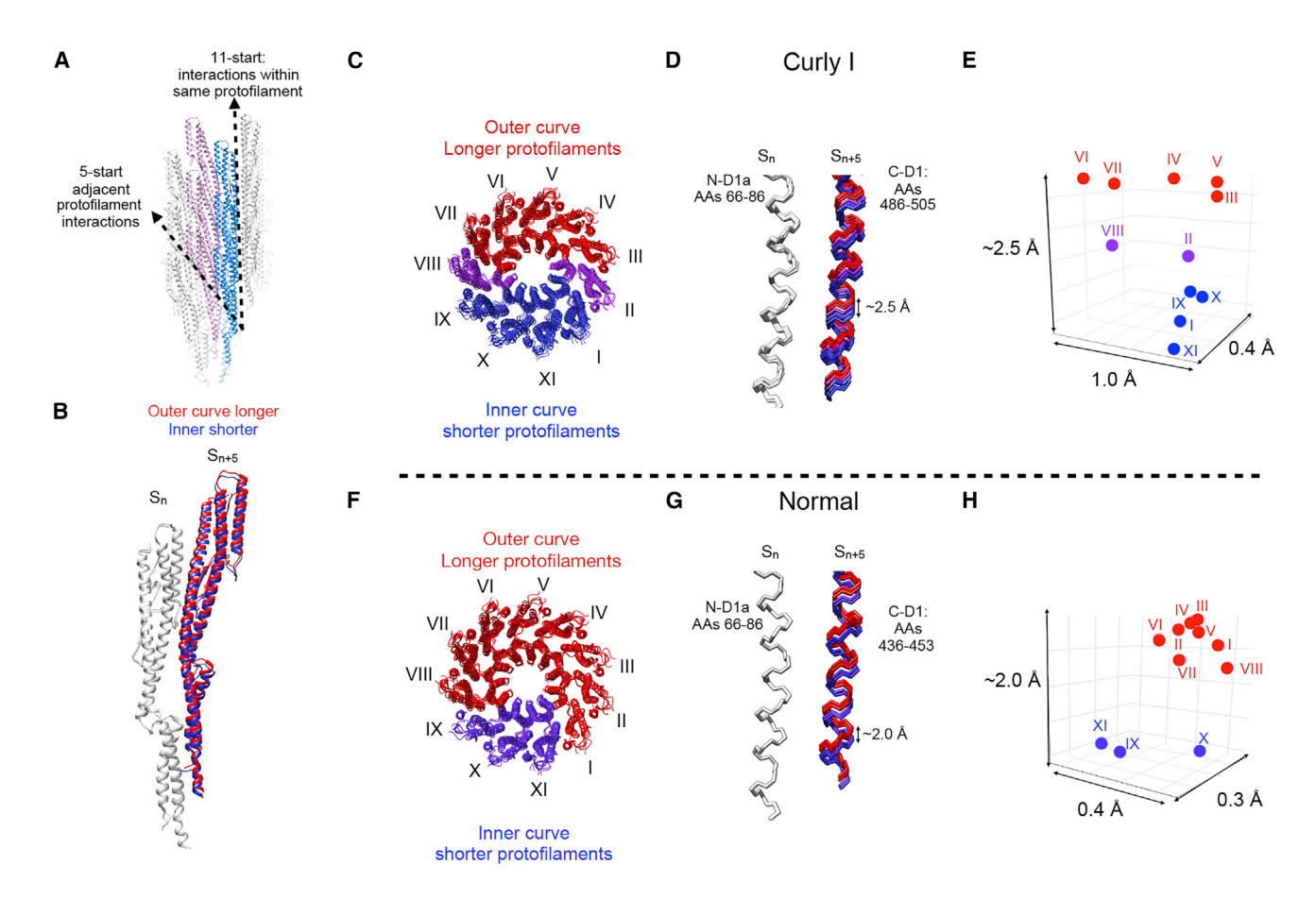


Figure 4. The 5-start interfacial switch of supercoiled bacterial flagellar filaments

- (A) Depiction showing 5-start and 11-start interfaces in a BFF. The 11-start interactions are any interactions between adjacent subunits along the same protofilament. The 5-start interactions occur between subunits on adjacent protofilaments.
- (B) Depiction of the alignment of subunits on adjacent protofilaments.
- (C) The protofilaments of the curly I flagellar filament colored by height along the 5-start interface. The longest protofilaments are colored red, and the shortest are colored blue. Protofilaments with intermediate interactions are colored purple
- (D) Close-up view of the switch interactions of N-D1a of a subunit S_n and C-D1 of an adjacent protofilament subunit S_{n+5} for all 11 interfaces. Each interface is aligned by the amino acids in N-D1 of subunit S_n. Subunits are colored according to the scheme in (C).
- (E) Three-dimensional plot of a single atom from the interfacial comparison in (D).
- (F) The protofilaments of the normal bacterial flagellar filament colored by height. The outer curve protofilaments are colored red, and the inner curve ones are
- (G) View of the switch interactions for the normal flagellar filament. The subunits S_{n+5} are colored according to the scheme in (F), and a maximal height of \sim 2.0 Å is present in the z dimension.
- (H) The three-dimensional coordinates of a single atom for all of the S_{n+5} subunits in the alignment from (G) are plotted. See also Figure S4.

same 10-start strand were conformationally similar to each other (Figure S6K). This led us to conclude that the AFFs are actually composed of 10 protofilaments (Figure 5F). We then aligned all of the 10 archaeal protofilaments by a subunit (S_n) and examined the differences that occur two subunits (S_{n+20}) further along the protofilaments (Figure 5G). Adjacent protofilaments were more similar to each other except for the two inner-most subunits in the curve (protofilaments I and IX, Figure 5H). We then built a model for the supercoiled REY15A flagellar filament in the same manner as for the bacterial filaments by aligning subunits from the same protofilament (Figure 5I). The resulting supercoil parameters were in good agreement with our negative-stain TEM observations (Figure 5A), and the waveform was left handed.

S. islandicus archaeal flagellar protofilament interactions contain a seam in the inner curve

The majority of the interactions between adjacent REY15A protofilaments resemble what is shown in Figure 6A, where isoleucine 26 of a subunit (S_{n+3}) is in close proximity to alanine 35 of a neighboring protofilament subunit (S_n). However, for the interface between two protofilaments labeled I and II (Figure 6B) in the inner region of the curve, there is a seam where protofilament I is shifted ~4 Å down the interface (Figure 6B blue inset) when





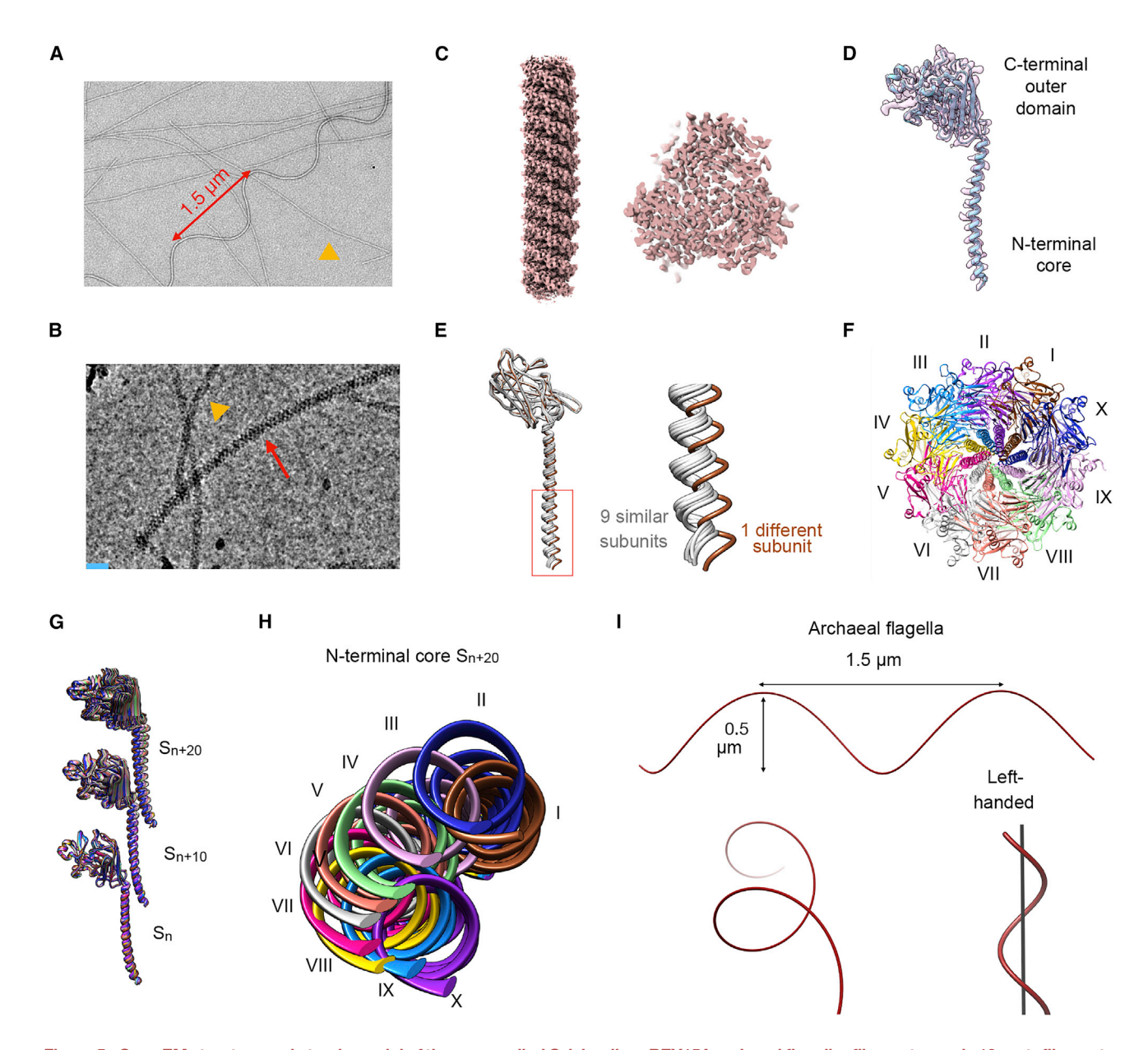


Figure 5. Cryo-EM structure and atomic model of the supercoiled S. islandicus REY15A archaeal flagellar filament reveals 10 protofilaments, each with a unique conformation

- (A) Negative-stain electron micrograph of the S. islandicus REY15A archaeal flagellar filament. The 1.5 µm pitch of the flagellum is shown with the red double arrow. An archaeal type IV pilus (T4P) is indicated with the yellow arrowhead.
- (B) Cryo-electron micrograph of the S. islandicus REY15A flagellar filament (red arrow). The scale bar is ∼20 nm.
- (C) The 3.4 Å resolution asymmetric cryo-EM reconstruction of the curved REY15A archaeal flagellar filament. A surface view of the structure is depicted on the left, whereas a top view is shown on the right.
- (D) Density map (light pink) and model (light blue) of a single REY15A archaeal flagellin.
- (E) Alignment of the 10 unique REY15A flagellin subunit models. The left image shows the full flagellin models. The right image shows a close-up view of the red boxed region.
- (F) The 10 protofilaments of the archaeal flagellar filament.
- (G) Alignment of the 10 archaeal flagellar protofilaments by subunit $S_{\rm n}$.
- (H) Same alignment from (C) with a top view of the N-terminal core of S_{n+20} . This view stops at the end of the N-terminal helix (residue 65).
- (I) Supercoiled model of the S. islandicus REY15A flagellar filament.

See also Figures S5 and S6.



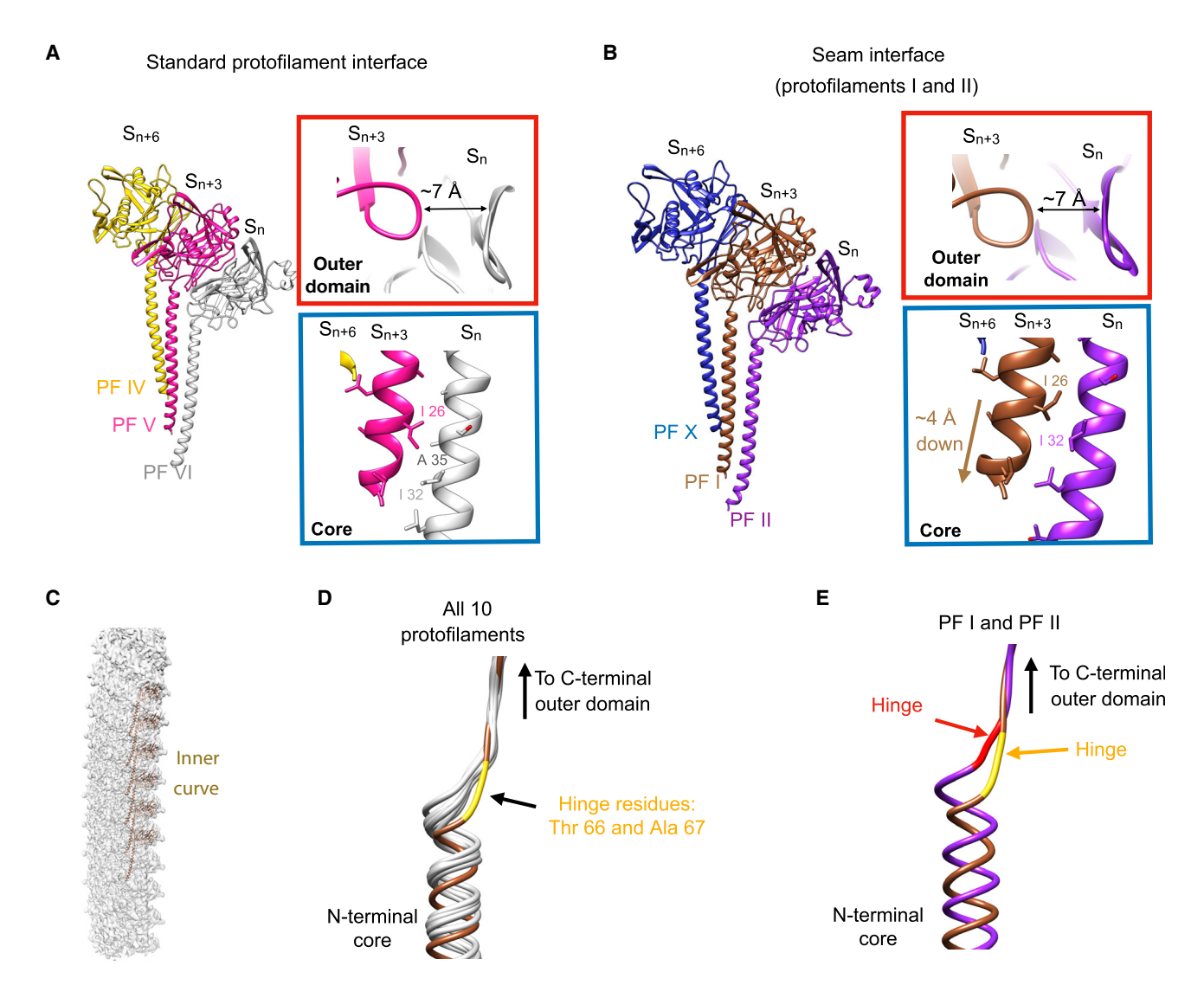


Figure 6. Subunit and protofilament interactions of the S. islandicus REY15A flagellar filament

(A) "Standard" 3-start interface between REY15A protofilaments. Three adjacent subunits from three adjacent protofilaments are shown. They are colored as in Figure 5F. The red inset shows the interaction between subunits S_{n+3} and S_n in their outer domains. A \sim 7 Å distance between the two backbones at this interface is indicated. The blue inset shows the interface between the subunits in the lpha-helical core.

- (B) The 3-start interface containing the seam subunit. The seam subunit is depicted in brown as S_{n+3} . In the red inset, the outer domain of the seam subunit (brown) and its standard neighbor (purple) have a distance of \sim 7 Å. In the blue inset, the α -helical core of the seam protofilament (brown) has shifted along the 3-start
- (C) Density map (light gray) with the model for the seam subunit (brown) on the inner part of the curve.
- (D) View of the linker region between the N-terminal helical core and the C-terminal outer domains of all 11 archaeal flagellin conformations aligned together.
- (E) The same view as in (D) with only the two inner curve protofilaments numbered I (brown) and II (purple). The linker hinge regions of residues 66 and 67 are colored gold and red for protofilaments I and II, respectively. See also Figure S6.

compared with the other nine standard interfaces. This results in the isoleucine 26 of subunit S_{n+3} moving closer to the isoleucine 32 of neighboring subunit S_n. These seam interactions do not occur in the outer domains (Figures 6A and 6B red insets), which are similar across all 3-start interfaces. The most conformationally different protofilament (I) is at the very inner region of the curve (Figure 6C), which is the location of the seam. We found that the major difference driving this ~4 Å shearing is the movement of the previously described archaeal flagellin "hinge" (Gambelli et al., 2022) (Figures 6D and 6E). This hinge is the linker between the N-terminal core and C-terminal outer domain and corresponds to threonine 66 and alanine 67. The hinge residues adopt different but similar conformations in 9 protofilaments and a drastically different conformation in the subunits belonging to protofilament I (Figure 6D). The two most conformationally distinct subunits are, thus, from protofilaments I and II, which





is caused by the movement of the hinge region downward in protofilament I relative to protofilament II (Figure 6E).

DISCUSSION

For many years, the understanding of BFF supercoiling came from a combination of low-resolution observations (Macnab, 1976) of supercoiled filaments coupled with higher resolution structures of straight mutant BFFs (Yonekura et al., 2003). The result of these studies was the two-state model (Calladine et al., 2013). With our cryo-EM structures of supercoiled BFFs and AFFs, we now provide a detailed view of the subunits enabling the supercoiling of prokaryotic flagella.

Most flagellar motors must be able to rotate a supercoiled filament in CCW and CW directions. For the BFF, the normal waveform is associated with running or straight swimming coupled to CCW rotation (Darnton et al., 2007). When one or several flagellar motors changes to CW rotation, the forces imposed by the motor reversal cause the switching from normal to semi-coiled or curly waveforms, and this screws the filament out of the bundle. For AFFs, altering buffer conditions such as pH and salt concentration change the waveforms of *Methanococcus voltae* AFFs (Bardy et al., 2002), but the visualization of rotating *Halobacterium salinarum* AFFs revealed little polymorphism or change in handedness upon motor rotational switching (Kinosita et al., 2016).

For the REY15A AFF, the linker hinge regions (residues 66 and 67) of all subunits exhibited a great degree of flexibility (Figure 6D). This hinge changes at the seam in the inner curvature of the supercoil. Flexibility of this linker region has been reported for other AFFs (Gambelli et al., 2022) as well as T4P (Wang et al., 2020); however, its relationship with protofilament conformations in supercoiled AFF was not described. The hinge may allow for the preservation of similar core domain contacts in 9 of the 10 interfaces and a seam in the 10th inner curvature interface (Figure 6). The REY15A flagellin has a larger C-terminal domain (~260 total residues) compared with other known archaeal flagellin structures (Gambelli et al., 2022; Meshcheryakov et al., 2019; Poweleit et al., 2016), which generates a very prominent 3-start helix on the surface of the filament (Figure S6F), with glycosylated residues forming a ridged surface along the 3-start helix (Figure S6G). We speculate that the extensive outer domain 3-start interactions and glycosylations in the REY15A AFF is an adaptation to the natural habitat of S. islandicus by providing additional stability in hot and acidic environments, similar to the glycosylation of S. islandicus LAL14/1 and S. solfataricus T4Ps (Wang et al., 2020; Wang et al., 2019).

The 11 conformations of the BFF protofilaments also change depending on the curvature of the waveform, with the protofilaments being more similar to each other in the normal waveform and more different in the curly I waveform. This is the result of the protofilaments increasing the degree to which they bend into the curve in the curly I compared with the normal state. Many of the components of the bacterial flagellum are homologous to those of type III secretion systems (T3SSs) (Abby and Rocha, 2012), and the lumen of the BFF functions as a channel for protein secretion (Nedeljković et al., 2021). The structure of the flagellar lumen is preserved in the superhelical states through

the conformational continuum of protofilament conformations. The larger differences in protofilament and subunit conformations between the curly I and normal structures (Figure 3) are the result of curvature and the need to preserve the structure of the flagellar lumen.

Considering the abrupt discontinuity in the arrangement of the flagellin subunits in the supercoiled state of the AFF, an analogy might be made to the hexameric Rho transcription-termination helicase. Although early low-resolution EM studies suggested that Rho formed a ring with a C6 symmetry (Yu et al., 2000), a high-resolution crystal structure revealed that the ring was actually a "lock washer" with a discontinuity between two of the subunits (Skordalakes and Berger, 2003). It is tempting to view wildtype archaeal and bacterial flagellins in a similar manner. For BFFs, which are assembled from subunits with multiple helices (Figure 7A), a straight filament with 10 coiled-coil subunits generating 10 identical protofilaments may be possible (Figure 7B). However, the subunits may not be able to generate a completed straight flagellar filament containing 11 protofilaments without considerable strain and clashes (Figure 7C). Thus, the supercoiled BFF states may indeed also reflect a minimum energy state where there are 11 unique protofilaments, with shorter ones on the inner curve and longer ones on the outside (Figure 7D). The situation might be similar for AFFs, but they are composed from a single α -helix in the core (Figure 7E), which might easily be able to assemble into a straight polymer containing nine identical protofilaments (Figure 7F). However, the addition of a 10th subunit to complete the AFF might be unable to assemble into a straight polymer due to clashes (Figure 7G). As a result, the minimum energy state of the AFF involves 10 protofilament states with a seam at the inner curve (Figure 7H).

Both the normal and curly I waveforms would, thus, represent the minimum energy state of the BFF under different conditions. BFFs adopt the normal waveform when they are rotated CCW. When the rotation of the motor switches to CW, the affected BFF breaks out of the bundle and frequently adopts the semicoiled waveform, followed by curly I. During CW rotation, the right-handed curly I form is, thus, the minimum energy state. This "two-step" transition involving semi-coiled and then curly I waveforms is likely due to the semi-coiled waveform being an intermediate between the normal and curly I waveforms.

Comparisons between higher resolution L- and R-state bacterial flagellins (Wang et al., 2017) reveal larger differences than between the flagellins in the supercoiled structures observed by us (Figures S7A–S7D), but these L versus R differences are still much smaller than those based upon lower resolution structures (Maki-Yonekura et al., 2010). It is possible that the L- and R-state switches prevent the shifting of 5-start interfacial interactions (Figures S7E and S7F) or subtle conformational switching of the flagellin in other key regions (Wang et al., 2017).

Similar to both AFFs and BFFs, the supercoiled bacterial flagellar hook contains unique conformational states for each protofilament (Kato et al., 2019; Shibata et al., 2019), whereas the flagellar hook protein, FlgE, shares no homology to either bacterial or archaeal flagellins. Notably, the conformations adopted by FlgE in the supercoiled structure are more drastically different (Figure S7G) from each other than either the bacterial (Figure S7H) or archaeal (Figure S7I) flagellins in their supercoiled



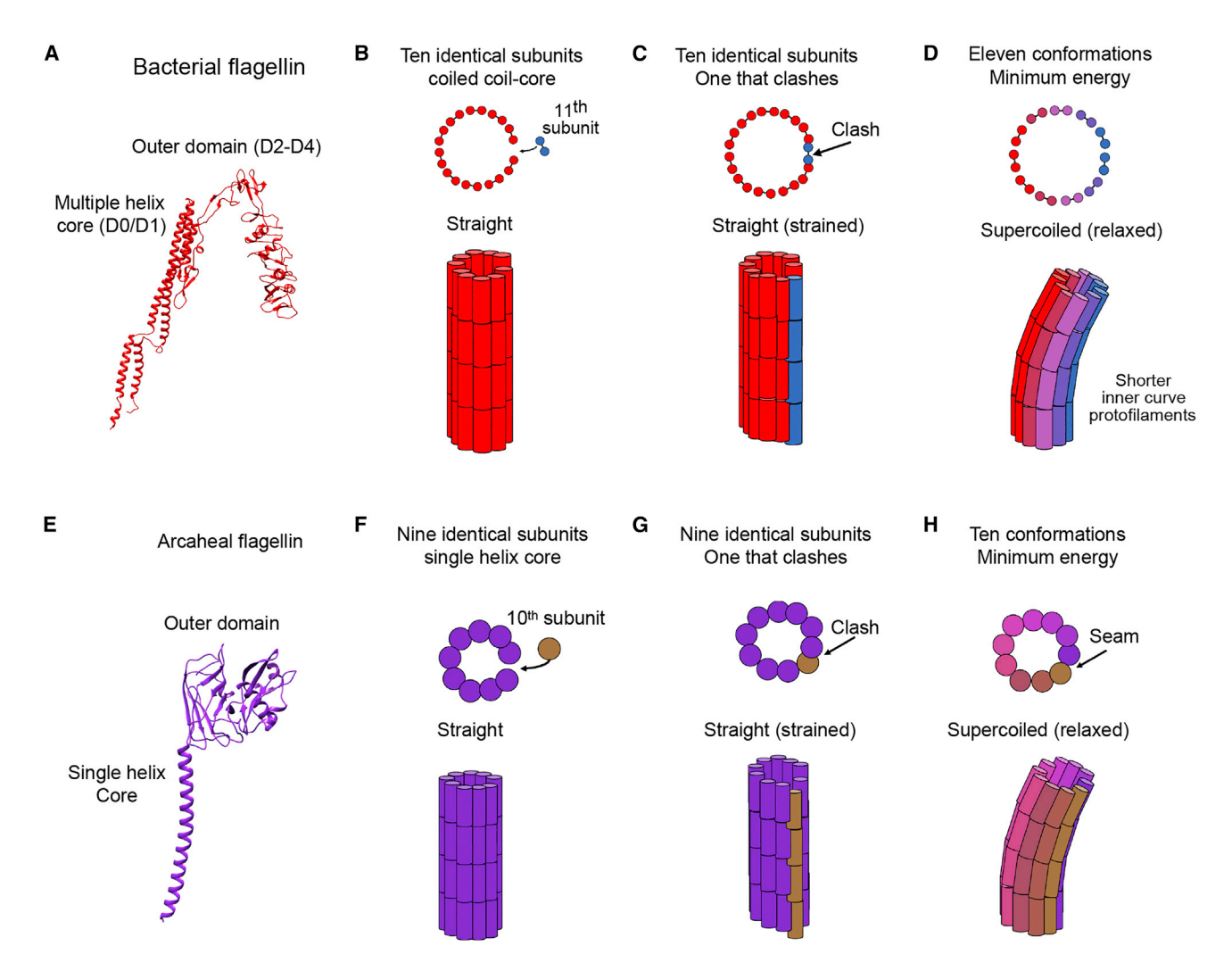


Figure 7. A comparison of the supercoiling of archaeal and bacterial flagellar filaments

(A) A single EPEC H6 flagellin.

- (B) Here, there are 11 protofilaments, and in the top view, the coiled-coil subunits are each represented by two circles connected by a line. The bottom image gives the side view of the filament, with subunits being represented as cylinders.
- (C) Representation showing how the addition of the 11th bacterial protofilament would result in clashes if the filament was straight.
- (D) The minimum energy state of the bacterial flagellar filament is supercoiled and has 11 protofilament conformations. The shortest protofilaments are blue, and the longest are red. The depicted supercoiled state is that of curly I.
- (E) A single REY15A archaeal flagellin.
- (F) Representation of 9 identical subunits (purple) assembling into a perfectly straight filament with nine straight protofilaments. Archaeal flagellar filaments, however, are assembled from 10 protofilaments. The top image is a top-down view of the filament, and circles represent the single α -helix for each subunit in the REY15A flagellar core.
- (G) Representation showing the addition of a 10th subunit (brown). The archaeal flagellar filament cannot assemble into a straight flagellum, as there would be
- (H) Representation of the minimum energy assembly of a supercoiled archaeal flagellum with 10 protofilaments each in a different conformation. Protofilaments are colored in the order of similarity, with the two extremes being purple and brown, which are the conformations most different from each other. See also Figure S7.

structures. This increased difference among flagellar hook protein conformations is likely due to the much greater curvature of the supercoiled flagellar polyhooks (Figure S7J) when compared with BFFs (Figure S7K) or AFFs (Figure S7L). The increased curvature of the supercoiled flagellar polyhook is likely reflective of the hook's function as a universal joint rather than a propeller.

Our data presented here show that convergent evolution between archaeal and bacterial flagella extends to the general mechanism underlying the flagellar supercoiling and, hence, motility of bacteria and archaea. These considerations raise new questions about the terminology. The archaeal flagellar system has been called the archaellum (Jarrell and Albers, 2012) based upon the notion that it has no homology with the bacterial





flagellar system. However, the bacterial flagellar system has no homology to eukaryotic flagella, such as the whipping tails of sperms (Gaffney et al., 2021) or protozoic trypanosomes (Langousis and Hill, 2014), yet these analogous structures are still called flagella in both bacteria and eukaryotes (Wirth, 2012). As such, it is our preference to refer to the structures presented in this paper as AFFs and BFFs. Despite the lack of homology between the structural components, the mechanisms of archaeal and bacterial flagellar supercoiling are analogous and examples of convergent evolution, much similar to how the wings of bees and bats have evolved independently.

Limitations of the study

Although, for BFFs, there has been an extensive analysis of mutations in various domains coupled with light microscopic visualization of flagellar filament waveforms, such data are virtually nonexistent for AFFs. Future studies would hopefully involve the mutagenesis of archaeal flagellins coupled with light microscopy and motility assays. Additionally, we acknowledge that the compressional forces caused by cryo-EM grid preparation could cause slight distortions in our structures. Nevertheless, this is likely a minimal source of error because of the accurate supercoiling parameters we obtain from our coarse-grained models. This study also considers only two of the experimentally observed supercoiled waveforms. Future studies would be required to further investigate how the protofilament and 5-start interactions change across the other experimentally observed waveforms.

STAR*METHODS

Detailed methods are provided in the online version of this paper and include the following:

- KEY RESOURCES TABLE
- RESOURCE AVAILABILITY
 - Lead contact
 - Materials availability
 - Data and code availability
- EXPERIMENTAL MODEL AND SUBJECT DETAILS
 - Bacterial strains and growth conditions
 - Archaeal strains and growth conditions
- METHOD DETAILS
 - O Preparation of EPEC H6 flagellar filaments
 - O Preparation of E. coli K-12 flagellar filaments
 - O Preparation of S. islandicus REY15A AFFs
 - O Preparation of C. jejuni flagellar filaments
 - Annealing experiments with BFFs
 - O Cryo-EM sample and grid preparation
 - CryoEM image acquisition
 - Helical reconstruction
 - Asymmetric reconstruction
 - Local resolution estimation
 - Model building
 - Determination of modeling error in comparisons of independently built subunits
 - Comparison of flagellin subunits

- Coarse-grained modeling of the supercoil of prokaryotic flagellar filaments
- Cryo-electron tomography
- QUANTIFICATION AND STATISTICAL ANALYSIS

SUPPLEMENTAL INFORMATION

Supplemental information can be found online at https://doi.org/10.1016/j.cell. 2022.08.009.

ACKNOWLEDGMENTS

This work was supported by NIH GM122150 (to E.H.E.). This work was also supported by U.S. Navy Work Unit (program 6000.RAD1.DA3.A0308, to F.P.). M.A.K.B. was supported by the Robert R. Wagner Fellowship and NIH grant T32 GM080186. The views expressed in this article reflect the results of research conducted by the authors and do not necessarily reflect the official policy or position of the Department of the Navy, Department of Defense, or the US Government. F.P. is a federal employee of the US Government, and this work was prepared as part of his official duties. Title 17 U.S.C. 105 provides that copyright protection under this title is not available for any work of the US Government. Title 17 U.S.C. 101 defines a US Government work as work prepared by a military service member or employee of the US Government as part of that person's official duties. Electron microscopy was performed at the Molecular Electron Microscopy Core at the University of Virginia.

AUTHOR CONTRIBUTIONS

E.H.E. and M.A.B.K. designed this study, while C.R.C., B.F.L., M.K., and F.W. provided additional suggestions for experiments. Various flagellar filament samples were provided by J.L., S.C., A.L.S., P.B., and C.E. under the guidance of M.K., G.F., B.E.S., and F.P. Cryo-EM analyses and reconstructions were performed by M.A.B.K. and R.R.S. Samples and grids were prepared for EM by M.A.B.K., R.R.S., F.W., and W.Z. The flagella annealing experiment was performed by M.A.B.K. Figures were prepared by M.A.B.K. and R.R.S. Manuscript was written by M.A.B.K., E.H.E, B.F.L., C.R.C., and B.E.S. Additional manuscript editing and revisions were provided by R.R.S., J.L., G.F., and M.K.

DECLARATION OF INTERESTS

The authors declare no competing interests.

Received: May 18, 2022 Revised: July 4, 2022 Accepted: August 4, 2022 Published: September 2, 2022

REFERENCES

Abby, S.S., and Rocha, E.P. (2012). The non-flagellar type III secretion system evolved from the bacterial flagellum and diversified into host-cell adapted systems. PLoS Genet. 8, e1002983. https://doi.org/10.1371/journal.pgen. 1002983.

Afonine, P.V., Klaholz, B.P., Moriarty, N.W., Poon, B.K., Sobolev, O.V., Terwilliger, T.C., Adams, P.D., and Urzhumtsev, A. (2018a). New tools for the analysis and validation of cryo-EM maps and atomic models. Acta Crystallogr. D Struct. Biol. 74, 814–840. https://doi.org/10.1107/S2059798318009324.

Afonine, P.V., Poon, B.K., Read, R.J., Sobolev, O.V., Terwilliger, T.C., Urzhumtsev, A., and Adams, P.D. (2018b). Real-space refinement in PHENIX for cryo-EM and crystallography. Acta Crystallogr. D Struct. Biol. 74, 531–544. https://doi.org/10.1107/S2059798318006551.

Asakura, S. (1970). Polymerization of flagellin and polymorphism of flagella. Adv. Biophys. 1, 99–155.

Bardy, S.L., Mori, T., Komoriya, K., Aizawa, S., and Jarrell, K.F. (2002). Identification and localization of flagellins FlaA and FlaB3 within flagella of





Methanococcus voltae. J. Bacteriol. 184, 5223-5233. https://doi.org/10.1128/ JB.184.19.5223-5233.2002.

Bayley, D.P., and Jarrell, K.F. (1998). Further evidence to suggest that archaeal flagella are related to bacterial type IV pili. J. Mol. Evol. 46, 370-373.

Blum, T.B., Filippidou, S., Fatton, M., Junier, P., and Abrahams, J.P. (2019). The wild-type flagellar filament of the firmicute Kurthia at 2.8 Å resolution in vivo. Sci. Rep. 9, 14948. https://doi.org/10.1038/s41598-019-51440-1.

Calladine, C.R. (1975). Construction of bacterial flagella. Nature 255, 121-124.

Calladine, C.R., Luisi, B.F., and Pratap, J.V. (2013). A "mechanistic" explanation of the multiple helical forms adopted by bacterial flagellar filaments. J. Mol. Biol. 425, 914-928. https://doi.org/10.1016/j.jmb.2012.12.007.

Calldine, C.R. (1978). Change of waveform in bacterial flagella: the role of mechanics at the molecular level. J. Mol. Biol. 118, 457-479. https://doi.org/10. 1016/0022-2836(78)90285-1.

Cohen-Krausz, S., and Trachtenberg, S. (2002). The structure of the archeabacterial flagellar filament of the extreme halophile Halobacterium salinarum R1M1 and its relation to eubacterial flagellar filaments and type IV pili. J. Mol. Biol. 321, 383-395. https://doi.org/10.1016/s0022-2836(02)00616-2.

Darnton, N.C., Turner, L., Rojevsky, S., and Berg, H.C. (2007). On torque and tumbling in swimming Escherichia coli. J. Bacteriol. 189, 1756-1764. https:// doi.org/10.1128/JB.01501-06.

Deng, L., Zhu, H., Chen, Z., Liang, Y.X., and She, Q. (2009). Unmarked gene deletion and host-vector system for the hyperthermophilic crenarchaeon Sulfolobus islandicus. Extremophiles 13, 735-746. https://doi.org/10.1007/ s00792-009-0254-2.

Egelman, E.H. (2000). A robust algorithm for the reconstruction of helical filaments using single-particle methods. Ultramicroscopy 85, 225-234. https:// doi.org/10.1016/S0304-3991(00)00062-0.

Emsley, P., Lohkamp, B., Scott, W.G., and Cowtan, K. (2010). Features and development of coot. Acta Crystallogr. D Biol. Crystallogr. 66, 486-501. https://doi.org/10.1107/S0907444910007493.

Erdem, A.L., Avelino, F., Xicohtencatl-Cortes, J., and Giron, J.A. (2007). Host protein binding and adhesive properties of H6 and H7 flagella of attaching and effacing Escherichia coli. J Bacteriol 189, 7426-7435.

Frank, J., Radermacher, M., Penczek, P., Zhu, J., Li, Y., Ladjadj, M., and Leith, A. (1996). Spider and WEB: processing and visualization of images in 3D electron microscopy and related fields. J. Struct. Biol. 116, 190-199. https://doi. org/10.1006/jsbi.1996.0030.

Gaffney, E.A., Ishimoto, K., and Walker, B.J. (2021). Modelling motility: the mathematics of spermatozoa. Front. Cell Dev. Biol. 9, 710825. https://doi. org/10.3389/fcell.2021.710825.

Gambelli, L., Isupov, M.N., Conners, R., McLaren, M., Bellack, A., Gold, V., Rachel, R., and Daum, B. (2022). An archaellum filament composed of two alternating subunits. Nat. Commun. 13, 710. https://doi.org/10.1038/s41467-022-

Ghosh, A., and Albers, S.V. (2011). Assembly and function of the archaeal flagellum. Biochem. Soc. Trans. 39, 64-69. https://doi.org/10.1042/

Guo, L., Brügger, K., Liu, C., Shah, S.A., Zheng, H., Zhu, Y., Wang, S., Lillestøl, R.K., Chen, L., Frank, J., et al. (2011). Genome analyses of icelandic strains of Sulfolobus islandicus, model organisms for genetic and virus-host interaction studies. J. Bacteriol. 193, 1672-1680. https://doi.org/10.1128/JB.01487-10.

Hyman, H.C., and Trachtenberg, S. (1991). Point mutations that lock Salmonella typhimurium flagellar filaments in the straight right-handed and lefthanded forms and their relation to filament superhelicity. J. Mol. Biol.

Jarrell, K.F., and Albers, S.V. (2012). The archaellum: an old motility structure with a new name. Trends Microbiol. 20, 307-312. https://doi.org/10.1016/j.

Jensen, K.F. (1993). The Escherichia coli K-12 "wild types" W3110 and MG1655 have an rph frameshift mutation that leads to pyrimidine starvation due to low pyrE expression levels. J Bacteriol 175, 3401-3407.

Jumper, J., Evans, R., Pritzel, A., Green, T., Figurnov, M., Ronneberger, O., Tunyasuvunakool, K., Bates, R., Žídek, A., Potapenko, A., et al. (2021). Highly accurate protein structure prediction with AlphaFold. Nature 596, 583-589. https://doi.org/10.1038/s41586-021-03819-2.

Kamiya, R., and Asakura, S. (1976). Helical transformations of Salmonella flagella in vitro. J. Mol. Biol. 106, 167-186. https://doi.org/10.1016/0022-2836(76)90306-5.

Kamiya, R., Hotani, H., and Asakura, S. (1982). Polymorphic transition in bacterial flagella. Symp. Soc. Exp. Biol. 35, 53-76.

Kanto, S., Okino, H., Aizawa, S., and Yamaguchi, S. (1991). Amino acids responsible for flagellar shape are distributed in terminal regions of flagellin. J. Mol. Biol. 219, 471-480. https://doi.org/10.1016/0022-2836(91)90187-b.

Kato, T., Makino, F., Miyata, T., Horváth, P., and Namba, K. (2019). Structure of the native supercoiled flagellar hook as a universal joint. Nat. Commun. 10, 5295. https://doi.org/10.1038/s41467-019-13252-9.

Khan, S., and Scholey, J.M. (2018). Assembly, functions and evolution of archaella, flagella and cilia. Curr. Biol. 28, R278-R292. https://doi.org/10.1016/j. cub.2018.01.085.

Kinosita, Y., Uchida, N., Nakane, D., and Nishizaka, T. (2016). Direct observation of rotation and steps of the archaellum in the swimming halophilic archaeon Halobacterium salinarum. Nat. Microbiol. 1, 16148. https://doi.org/ 10.1038/nmicrobiol.2016.148.

Kremer, J.R., Mastronarde, D.N., and McIntosh, J.R. (1996). Computer visualization of three-dimensional image data using IMOD. J. Struct. Biol. 116, 71-76. https://doi.org/10.1006/jsbi.1996.0013.

Kreutzberger, M.A.B., Ewing, C., Poly, F., Wang, F., and Egelman, E.H. (2020). Atomic structure of the Campylobacter jejuni flagellar filament reveals how ϵ Proteobacteria escaped toll-like receptor 5 surveillance. Proc. Natl. Acad. Sci. USA 117, 16985-16991. https://doi.org/10.1073/pnas.2010996117.

Kreutzberger, M.A.B., Sobe, R.C., Sauder, A.B., Chatterjee, S., Peña, A., Wang, F., Giron, J.A., Kiessling, V., Costa, T.R.D., Conticello, V.P., et al. (2022). Flagellin outer domain dimerization modulates motility in pathogenic and soil bacteria from viscous environments. Nat. Commun. 13, 1422. https://doi.org/10.1038/s41467-022-29069-y.

Langousis, G., and Hill, K.L. (2014). Motility and more: the flagellum of Trypanosoma brucei. Nat. Rev. Microbiol. 12, 505-518. https://doi.org/10.1038/ nrmicro3274.

Macnab, R.M. (1976). Examination of bacterial flagellation by dark-field microscopy. J. Clin. Microbiol. 4, 258-265. https://doi.org/10.1128/jcm.4.3.258-265.1976.

Macnab, R.M. (2003). How bacteria assemble flagella. Annu. Rev. Microbiol. 57, 77-100. https://doi.org/10.1146/annurev.micro.57.030502.090832.

Makarova, K.S., Koonin, E.V., and Albers, S.V. (2016). Diversity and evolution of type IV pili systems in archaea. Front. Microbiol. 7, 667. https://doi.org/10. 3389/fmicb.2016.00667.

Maki-Yonekura, S., Yonekura, K., and Namba, K. (2010). Conformational change of flagellin for polymorphic supercoiling of the flagellar filament. Nat. Struct. Mol. Biol. 17, 417-422. https://doi.org/10.1038/nsmb.1774.

Mastronarde, D.N., and Held, S.R. (2017). Automated tilt series alignment and tomographic reconstruction in IMOD. J. Struct. Biol. 197, 102-113. https://doi. org/10.1016/j.jsb.2016.07.011.

Meshcheryakov, V.A., Shibata, S., Schreiber, M.T., Villar-Briones, A., Jarrell, K.F., Aizawa, S.I., and Wolf, M. (2019). High-resolution archaellum structure reveals a conserved metal-binding site. EMBO Rep. 20. https://doi.org/10. 15252/embr.201846340.

Montemayor, E.J., Ploscariu, N.T., Sanchez, J.C., Parrell, D., Dillard, R.S., Shebelut, C.W., Ke, Z., Guerrero-Ferreira, R.C., and Wright, E.R. (2021). Flagellar structures from the bacterium Caulobacter crescentus and Implications for phage φCbK predation of multiflagellin bacteria. J. Bacteriol. 203, e00399-20. https://doi.org/10.1128/JB.00399-20.

Nedeljković, M., Sastre, D.E., and Sundberg, E.J. (2021). Bacterial flagellar filament: a supramolecular multifunctional nanostructure. Int. J. Mol. Sci. 22, 7521. https://doi.org/10.3390/ijms22147521.





Noske, A.B., Costin, A.J., Morgan, G.P., and Marsh, B.J. (2008). Expedited approaches to whole cell electron tomography and organelle mark-up in situ in high-pressure frozen pancreatic islets. J. Struct. Biol. 161, 298-313. https:// doi.org/10.1016/j.jsb.2007.09.015.

O'Brien, E.J., and Bennett, P.M. (1972). Structure of straight flagella from a mutant Salmonella. J. Mol. Biol. 70, 133-152. https://doi.org/10.1016/0022-2836(72)90168-4

Ortega, D., and Beeby, M. (2021). How did the archaellum get its rotation? Front. Microbiol. 12, 803720. https://doi.org/10.3389/fmicb.2021.803720.

Pazour, G.J., Agrin, N., Leszyk, J., and Witman, G.B. (2005). Proteomic analysis of a eukaryotic cilium. J. Cell Biol. 170, 103-113. https://doi.org/10. 1083/jcb.200504008.

Pettersen, E.F., Goddard, T.D., Huang, C.C., Couch, G.S., Greenblatt, D.M., Meng, E.C., and Ferrin, T.E. (2004). UCSF Chimeras-a visualization system for exploratory research and analysis. J. Comput. Chem. 25, 1605-1612. https://doi.org/10.1002/jcc.20084.

Pettersen, E.F., Goddard, T.D., Huang, C.C., Meng, E.C., Couch, G.S., Croll, T.I., Morris, J.H., and Ferrin, T.E. (2021). UCSF ChimeraX: structure visualization for researchers, educators, and developers. Protein Sci. 30, 70-82. https://doi.org/10.1002/pro.3943.

Poweleit, N., Ge, P., Nguyen, H.H., Loo, R.R., Gunsalus, R.P., and Zhou, Z.H. (2016). CryoEM structure of the Methanospirillum hungatei archaellum reveals structural features distinct from the bacterial flagellum and type IV pilus. Nat. Microbiol. 2, 16222. https://doi.org/10.1038/nmicrobiol.2016.222.

Punjani, A., Rubinstein, J.L., Fleet, D.J., and Brubaker, M.A. (2017). cryo-SPARC: algorithms for rapid unsupervised cryo-EM structure determination. Nat. Methods 14, 290-296. https://doi.org/10.1038/nmeth.4169.

Rice, W.J., Cheng, A., Noble, A.J., Eng, E.T., Kim, L.Y., Carragher, B., and Potter, C.S. (2018). Routine determination of ice thickness for cryo-EM grids. J. Struct. Biol. 204, 38-44. https://doi.org/10.1016/j.jsb.2018.06.007.

Shibata, S., Matsunami, H., Aizawa, S.I., and Wolf, M. (2019). Torque transmission mechanism of the curved bacterial flagellar hook revealed by cryo-EM. Nat. Struct. Mol. Biol. 26, 941-945. https://doi.org/10.1038/s41594-019-

Skordalakes, E., and Berger, J.M. (2003). Structure of the Rho transcription terminator: mechanism of mRNA recognition and helicase loading. Cell 114,

Sonnhammer, E.L., von Heijne, G., and Krogh, A. (1998). A hidden Markov model for predicting transmembrane helices in protein sequences. Proc. Int. Conf. Intell. Syst. Mol. Biol. 6, 175-182.

Subramaniam, S., Earl, L.A., Falconieri, V., Milne, J.L., and Egelman, E.H. (2016). Resolution advances in cryo-EM enable application to drug discovery. Curr. Opin. Struct. Biol. 41, 194-202. https://doi.org/10.1016/j.sbi.2016.

Thomas, N.A., Bardy, S.L., and Jarrell, K.F. (2001). The archaeal flagellum: a different kind of prokaryotic motility structure. FEMS Microbiol. Rev. 25, 147-174. https://doi.org/10.1111/j.1574-6976.2001.tb00575.x.

Trachtenberg, S., and DeRosier, D.J. (1988). Three-dimensional reconstruction of the flagellar filament of Caulobacter crescentus: A flagellin lacking the outer domain and its amino acid sequence lacking an internal segment. J. Mol. Biol. 202, 787-808. https://doi.org/10.1016/0022-2836(88)90559-1.

Turner, L., Ryu, W.S., and Berg, H.C. (2000). Real-time imaging of fluorescent flagellar filaments. J. Bacteriol. 182, 2793–2801. https://doi.org/10.1128/JB. 182.10.2793-2801.2000.

Wang, F., Baquero, D.P., Su, Z., Beltran, L.C., Prangishvili, D., Krupovic, M., and Egelman, E.H. (2020). The structures of two archaeal type IV pili illuminate evolutionary relationships. Nat. Commun. 11, 3424. https://doi.org/10.1038/ s41467-020-17268-4.

Wang, F., Burrage, A.M., Postel, S., Clark, R.E., Orlova, A., Sundberg, E.J., Kearns, D.B., and Egelman, E.H. (2017). A structural model of flagellar filament switching across multiple bacterial species. Nat. Commun. 8, 960. https://doi. org/10.1038/s41467-017-01075-5.

Wang, F., Cvirkaite-Krupovic, V., Kreutzberger, M.A.B., Su, Z., de Oliveira, G.A.P., Osinski, T., Sherman, N., DiMaio, F., Wall, J.S., Prangishvili, D., et al. (2019). An extensively glycosylated archaeal pilus survives extreme conditions. Nat. Microbiol. 4, 1401-1410. https://doi.org/10.1038/s41564-019-0458-x

Williams, C.J., Headd, J.J., Moriarty, N.W., Prisant, M.G., Videau, L.L., Deis, L.N., Verma, V., Keedy, D.A., Hintze, B.J., Chen, V.B., et al. (2018). MolProbity: more and better reference data for improved all-atom structure validation. Protein Sci. 27, 293-315. https://doi.org/10.1002/pro.3330.

Wirth, R. (2012). Response to Jarrell and Albers: seven letters less does not say more. Trends Microbiol. 20, 511-512. https://doi.org/10.1016/j.tim.2012.

Yamashita, I., Hasegawa, K., Suzuki, H., Vonderviszt, F., Mimori-Kiyosue, Y., and Namba, K. (1998). Structure and switching of bacterial flagellar filaments studied by X-ray fiber diffraction. Nat. Struct. Biol. 5, 125-132. https://doi.org/ 10.1038/nsb0298-125

Yonekura, K., Maki-Yonekura, S., and Namba, K. (2003). Complete atomic model of the bacterial flagellar filament by electron cryomicroscopy. Nature 424, 643-650. https://doi.org/10.1038/nature01830.

Yoshioka, K., Aizawa, S., and Yamaguchi, S. (1995). Flagellar filament structure and cell motility of Salmonella typhimurium mutants lacking part of the outer domain of flagellin. J. Bacteriol. 177, 1090-1093. https://doi.org/10. 1128/jb.177.4.1090-1093.1995.

Yu, X., Horiguchi, T., Shigesada, K., and Egelman, E.H. (2000). Three-dimensional reconstruction of transcription termination factor rho: orientation of the N-terminal domain and visualization of an RNA- binding site. J. Mol. Biol. 299, 1279-1287.

Zarschler, K., Janesch, B., Pabst, M., Altmann, F., Messner, P., and Schäffer, C. (2010). Protein tyrosine O-glycosylation-a rather unexplored prokaryotic glycosylation system. Glycobiology 20, 787-798. https://doi.org/10.1093/glycob/cwq035.





STAR***METHODS**

KEY RESOURCES TABLE

REAGENT or RESOURCE	SOURCE	IDENTIFIER
Bacterial and virus strains		
EPEC ICC526 (EPEC O127:H6 ΔbfpA + ΔespA)	Erdem et al., 2007	N/A
Sarccharolobus islandicus REY15A	Guo et al., 2011	N/A
Escherichia coli K-12 strain MG1655	Jensen, 1993	N/A
Chemicals, peptides, and recombinant proteins		
Bacto tryptone	Gibco	Cat #: 211705
Sodium chloride (NaCl)	Fisher Scientific	CAS #: 7647-14-5
Tris base	Fisher Scientific	CAS #: 77-86-1
EDTA	Sigma-Aldrich	Cat #: 10378
Sucrose	Sigma-Aldrich	Cat #: S0389
Calcium chloride	Sigma-Aldrich	Cat #: 21115
LB broth	Thermo-Fisher Scientific	Cat #: R453642
Phosphotungstic acid (PTA)	Electron Microscopy Sciences	Cat #: 19502-1
Uranyl acetate solution	Electron Microscopy Sciences	Cat #: 22400-2
HEPES	Fisher Scientific	Cat #: BP310-100
Deposited data		
EPEC H6 Curly I helical EM map	This paper	EMD-26995
EPEC H6 Curly I asymmetric EM Map (384x384)	This paper	EMD-27008
EPEC H6 Curly I asymmetric EM map (624x624)	This paper	EMD-27029
EPEC H6 Curly I asymmetric EM map (624x624) EPEC H6 Curly I model	This paper This paper	PDB 8CVI
EPEC H6 Curly I model	This paper	PDB 8CVI
EPEC H6 Curly I model EPEC H6 Normal helical EM map EPEC H6 Normal asymmetric EM map	This paper This paper This paper	PDB 8CVI EMD- 27064 EMD-27076
EPEC H6 Curly I model EPEC H6 Normal helical EM map	This paper This paper	PDB 8CVI EMD- 27064
EPEC H6 Curly I model EPEC H6 Normal helical EM map EPEC H6 Normal asymmetric EM map EPEC H6 Normal model E. coli K-12 Normal helical EM map	This paper This paper This paper This paper	PDB 8CVI EMD- 27064 EMD-27076 PDB-8CYE
EPEC H6 Curly I model EPEC H6 Normal helical EM map EPEC H6 Normal asymmetric EM map EPEC H6 Normal model E. coli K-12 Normal helical EM map	This paper This paper This paper This paper This paper This paper	PDB 8CVI EMD- 27064 EMD-27076 PDB-8CYE EMD-27059
EPEC H6 Curly I model EPEC H6 Normal helical EM map EPEC H6 Normal asymmetric EM map EPEC H6 Normal model E. coli K-12 Normal helical EM map E. coli K-12 Normal asymmetric EM map	This paper	PDB 8CVI EMD- 27064 EMD-27076 PDB-8CYE EMD-27059 EMD-27060
EPEC H6 Curly I model EPEC H6 Normal helical EM map EPEC H6 Normal asymmetric EM map EPEC H6 Normal model E. coli K-12 Normal helical EM map E. coli K-12 Normal asymmetric EM map E. coli K-12 Normal model	This paper	PDB 8CVI EMD- 27064 EMD-27076 PDB-8CYE EMD-27059 EMD-27060 PDB 8CXM
EPEC H6 Curly I model EPEC H6 Normal helical EM map EPEC H6 Normal asymmetric EM map EPEC H6 Normal model E. coli K-12 Normal helical EM map E. coli K-12 Normal asymmetric EM map E. coli K-12 Normal model S. islandicus REY15A AFF helical EM map	This paper	PDB 8CVI EMD- 27064 EMD-27076 PDB-8CYE EMD-27059 EMD-27060 PDB 8CXM EMD-27065
EPEC H6 Curly I model EPEC H6 Normal helical EM map EPEC H6 Normal asymmetric EM map EPEC H6 Normal model E. coli K-12 Normal helical EM map E. coli K-12 Normal asymmetric EM map E. coli K-12 Normal model S. islandicus REY15A AFF helical EM map S. islandicus REY15A AFF asymmetric EM map	This paper	PDB 8CVI EMD- 27064 EMD-27076 PDB-8CYE EMD-27059 EMD-27060 PDB 8CXM EMD-27065 EMD-27026
EPEC H6 Curly I model EPEC H6 Normal helical EM map EPEC H6 Normal asymmetric EM map EPEC H6 Normal model E. coli K-12 Normal helical EM map E. coli K-12 Normal asymmetric EM map E. coli K-12 Normal model S. islandicus REY15A AFF helical EM map S. islandicus REY15A AFF asymmetric EM map S. islandicus REY15A AFF model	This paper	PDB 8CVI EMD- 27064 EMD-27076 PDB-8CYE EMD-27059 EMD-27060 PDB 8CXM EMD-27065 EMD-27026 PDB-8CWM

(Continued on next page)





Continued		
REAGENT or RESOURCE	SOURCE	IDENTIFIER
S. typhimurium flagellar hook curved model	Shibata et al., 2019	PDB 6K3I
EPEC H6 helical atomic model	Kreutzberger et al., 2022	PDB 7SN7
Software and algorithms		
cryoSPARC	Punjani et al., 2017	https://cryosparc.com
Chimera	Pettersen et al., 2004	https://www.cgl.ucsf.edu/chimera
Coot	Emsley et al., 2010	https://www2.mrc-lmb.cam.ac.uk/ personal/pemsley/coot
MolProbity	Williams et al., 2018	http://molprobity.biochem.duke.edu
AlphaFold2	Jumper et al., 2021	https://alphafold.ebi.ac.uk
Spider	Frank et al., 1996	https://joachimfranklab.org/research/software/
Imod	Kremer et al., 1996	https://bio3d.colorado.edu/imod/

RESOURCE AVAILABILITY

Lead contact

Further information and requests for resources and reagents should be directed to and will be fulfilled by the lead contact, Edward H. Egelman, egelman@virginia.edu.

Materials availability

New and unique reagents were not generated by this study.

Data and code availability

- The helical EPEC H6 Curly I EM map is deposited as EMD-26995. The asymmetric EPEC H6 Curly I map and model are deposited as EMD-27008 and PDB 8CVI respectively. The longer EPEC H6 curly 1 map is deposited as EMD-27029. The EPEC H6 Normal helical EM map is deposited as EMD-27064. The EPEC H6 Normal asymmetric map and model are deposited as EMD-27076 and PDB 8CYE respectively. The E. coli K-12 Normal helical map is deposited as EMD-27059. The asymmetric E. coli K-12 Normal map and model are deposited as EMD-27060 and PDB 8CXM respectively. The S. islandicus REY15A helical map is deposited as EMD-27065. The asymmetric S. islandicus REY15A map and model are deposited as EMD-27026 and PDB 8CWM respectively.
- Original code is not reported in this paper.
- Any additional information required to reanalyze the data reported in this paper is available from the lead contact upon request.

EXPERIMENTAL MODEL AND SUBJECT DETAILS

Bacterial strains and growth conditions

E. coli K12 strain MG1655 (motile variant) was grown overnight in LB (1% tryptone, 0.5% yeast extract and 0.5% NaCl) at 37°C. The stationary culture was diluted 1:200 in 800 mL LB and grown to an OD₆₀₀ between 1.0 and 1.4. Cells were harvested by centrifugation for 8 minutes at 8,000 x g and suspended in 100 mL motility buffer (0.5 mM CaCl₂, 0.1 mM EDTA, 20 mM HEPES [pH 7.2]). EPEC ICC526 (EPEC O127:H6 Δ*bfpA* + Δ*espA*) cells carrying *pflhDC* were grown to an OD₆₀₀ of 0.6 and then induced with 0.5 mM isopropyl β-D-1-thiogalactopyranoside (IPTG) resulting in flagella expression (Kreutzberger et al., 2022). *Campylobacter jejuni* cells were cultured in Mueller Hinton Broth at 37°C (Kreutzberger et al., 2020).

Archaeal strains and growth conditions

S. islandicus REY15A (Guo et al., 2011) was grown aerobically with shaking (145 rpm) at 75 °C in STV medium containing mineral salts (M), 0.2% (wt/vol) sucrose (S), 0.2% (wt/vol) tryptone (T), a mixed vitamin solution (V) (Deng et al., 2009).

METHOD DETAILS

Preparation of EPEC H6 flagellar filaments

The EPEC H6 flagellar filaments were prepared as previously published (Kreutzberger et al., 2022). For the Curly I EPEC H6 sample the final buffer concentration was 1 M Tris/HCl 100 mM NaCl pH 6.5. For the Normal EPEC H6 sample the final buffer concentration was 50 mM Tris/HCl 75 mM NaCl pH 7.4.





Preparation of E. coli K-12 flagellar filaments

Flagella were sheared from cells by agitation in a mixer at full speed for 20 seconds and separated by three centrifugation steps: one at 8,000 x g for 7 minutes, followed by two at 15,000 x g for 15 minutes at 4°C. Purified flagella were then sedimented at 87,000 x g for 2 hours at 4°C, washed with motility buffer, and suspended in 200 mL motility buffer. Purity of flagellar filaments was analyzed by SDS-PAGE.

Preparation of S. islandicus REY15A AFFs

S. islandicus REY15A (Guo et al., 2011) was grown aerobically with shaking (145 rpm) at 75 °C in STV medium containing mineral salts (M), 0.2% (wt/vol) sucrose (S), 0.2% (wt/vol) tryptone (T), a mixed vitamin solution (V) (Deng et al., 2009). For isolation of flagellar filaments, REY15A cells were inoculate into 300 ml of MTSV medium at an initial OD₆₀₀ of 0.05 and cultivated for 18 h. Once cooled down to room temperature, the cell culture was vortexed to shear off the flagellar filaments from the cell surface. The cells were removed by centrifugation at 8,000 rpm for 20 min and the flagellar filaments were pelleted from the supernatant by ultra-centrifugation (Type 45Ti rotor, 40,000 rpm) at 10 °C for 2 h.

Preparation of C. jejuni flagellar filaments

Wild type C. jejuni 81-176 flagellar filaments were prepared as published (Kreutzberger et al., 2020) with filaments using bead beating and centrifugation to pellet the flagellar filaments and other cellular debris.

Annealing experiments with BFFs

Diluted 100 μL samples of bacterial flagella were heated at 55 °C for 30 minutes. The samples were then allowed to cool at room temperature for one hour. Samples before and after the annealing experiment were stained on continuous carbon EM grids using 1% phosphotungstic acid pH 7. The negatively stained samples were then imaged with a Technai T12 microscope operating at an accelerating voltage of 80 keV.

Cryo-EM sample and grid preparation

The cryo-EM grids were prepared for imaging as described previously (Kreutzberger et al., 2020; Kreutzberger et al., 2022). Samples were plunge frozen using either a Vitrobot Mark IV or a Leica EM GP. For the Vitrobot 3.5-4 μL of sample was applied to the grid and all blot times were 3.5 seconds and the blot forces ranged from 3 to 6. For the Leica 2.5-3 µL of sample was applied to the grid and the blot times were 3.5 S while blot distances ranged from 214-217.

CryoEM image acquisition

Images were acquired on a Titan Krios equipped with a K3 direct electron detector using a physical pixel size of 1.08 Å/pixel. The acerating voltage was 300 keV.

Helical reconstruction

Helical reconstruction of flagellar filaments was performed in Spider (Frank et al., 1996) using the iterative helical real space reconstruction algorithm (Egelman, 2000) and also performed in cryoSPARC (Punjani et al., 2017) with similar results.

Asymmetric reconstruction

Flagellar filaments were reconstructed asymmetrically using cryoSPARC (Punjani et al., 2017) in a series of steps. First a low-resolution helical volume (\sim 20-50 Å) was used as the initial volume for homogenous refinement. For all structures this initial round of homogenous refinement showed no curvature in the volume and still appeared largely helical. The particles and mask from this job were then used as inputs for a 3D variability job. The results from this job were reconstructed into 3D variability clusters and the highest resolution cluster with a curved volume was used for subsequent steps. To the best of our knowledge the volumes reconstructed from the 3D variability job represented a sort of "constrained" ab initio reconstruction, as no starting volume was used. However, a mask with general flagella features was as well as the particles containing the alignments parameters from the previous job. For the EPEC H6 reconstructions, a static mask consisting of just the core domains D0 and D1 was used for all steps, while for the E. coli K-12 and S. islandicus REY15A structures a mask consisting of the entire volume was used.

For some of our structures we found the curvature was present in the reconstruction from 3D variability but absent after taking these results as inputs for homogenous refinement. For best results, the chosen cluster of particles and its corresponding volume from 3D variability display was used as an input for a local refinement job with shifts constrained from 5-20 Å and rotational searches from 5-20° depending on the sample being imaged. These results were the used as inputs for local CTF correction followed by a second round of local refinement. For the Curly I EPEC H6 structure we were able to reconstruct curved volumes to 3.4 Å using a particles box size of 384 x 384 pixels and to \sim 4.0 Å (3.7 Å with 0.143 GFSC) using a box size of 624x624 pixels. The \sim 3 radians/ μ m curvature of the curly I was present in both structures, however smaller 384 x 384 box sizes for the Normal BFFs as well as the S. islandicus REY15A AFF produced straight volumes with little to no evidence of curvature. The EPEC H6 Normal and S. islandicus REY15A volumes were reconstructed using 624x624 particles boxes. The E. coli K-12 structure was reconstructed with a box size of 512x512.





Local resolution estimation

Local resolution maps were generated in cryoSPARC and visualized using ChimeraX (Pettersen et al., 2021).

Model building

The core domains D0 and D1 of the previously published EPEC H6 model (7SN7) was used as the initial subunit model for the Curly I and Normal EPEC H6 structures. AlphaFold (Jumper et al., 2021) was used to generate the starting models for the E. coli K-12 and S. islandicus REY15A flagellin models. For the REY15A AlphaFold model the secondary for each domain was predicted accurately, however the orientation of the C-terminal outer domain relative to the N-terminal core was incorrect. This makes sense because the model could not have accounted for the polymerization of the monomer into a filament. Modeling for each flagellar filament was initiated by fitting a single subunit into each protofilament using UCSF Chimera (Pettersen et al., 2004), and then refining each model using Coot (Emsley et al., 2010). For each protofilament the subunit initially fit and refined into a protofilament was copied (at least 3 copies each) and each copy was then fit into adjacent subunits along the same protofilament. Each subunit from each protofilament was refined individually in Coot and then each protofilament was refined using real-space refinement in Phenix (Afonine et al., 2018b). For each structure the 11 bacterial or 10 archaeal protofilament models were then combined together into a single model for that flagellar filament, which was subsequently refined in Phenix. The quality of the model was determined using Molprobity (Williams et al., 2018).

Determination of modeling error in comparisons of independently built subunits

To determine the extent to which we could interpret differences between subunits on the same or adjacent protofilaments, we conducted an experiment to predict the error of fitting a subunit into a map. We took a small segment of the H6 curly model in domain D1 (Figure S3I) and created 10 copies. To each, a different set of shifts in x, y, and z was applied (Figure S3J), with a mean rms shift of 2.6 Å. We then took the shifted models and used Phenix real space refinement to fit them into the corresponding region of the density map (Figure S3K). The C_{α} backbones of the 10 models were all quite similar after refinement (Figure S3L), and the average backbone rmsd value for the shifted models compared to the starting model was 0.2 Å. This estimate of the uncertainty in our models provided confidence that the detected structural differences between protein subunits are true conformational differences.

Comparison of flagellin subunits

All comparisons between flagellin subunits through structural alignments were generated with the matchmaker function in UCSF Chimera. The 3-dimensional plot shown in Figures 4E and 4H was generated using the free version of Plotly Chart Studio.

Coarse-grained modeling of the supercoil of prokaryotic flagellar filaments

For each flagellar filament model only a few atoms from each domain were kept for the coarse-grained model. All other atoms were deleted. The atomic radii of the alpha carbons were increased by ~20 Å to represent the flagellin subunits as large spheres. The chains of inner-most (lowest resolution) and outer-most (highest resolution) curve protofilaments were aligned in UCSF Chimera according to the scheme from Figure S7.

Cryo-electron tomography

A 5 μL aliquot of 10 nM BSA Gold Tracer (Electron Microscopy SciencesTM) was added to 10 μL of C. jejuni flagellar filaments. Grids were prepared in an identical fashion to all other flagellar filaments samples except that 300 copper mesh C-flat holey carbon grids were used with 2 μm x 2μm hole size. Tilt series were collected from -60° to +60° tilt with 1.5° degrees between each image and a dose of 4.2 e⁻/Å². Tomograms were generated using Etomo (Mastronarde and Held, 2017), which is part of the IMOD processing suite (Kremer et al., 1996). Segmentation of the flagellar filaments was then performed to better visualize them in 3-dimensions (Noske et al., 2008).

QUANTIFICATION AND STATISTICAL ANALYSIS

The quantification and statistical analyses are integral parts of the software and algorithms used, cryoSPARC for the generation of the maps and Phenix for the generation of the atomic models.



Supplemental figures

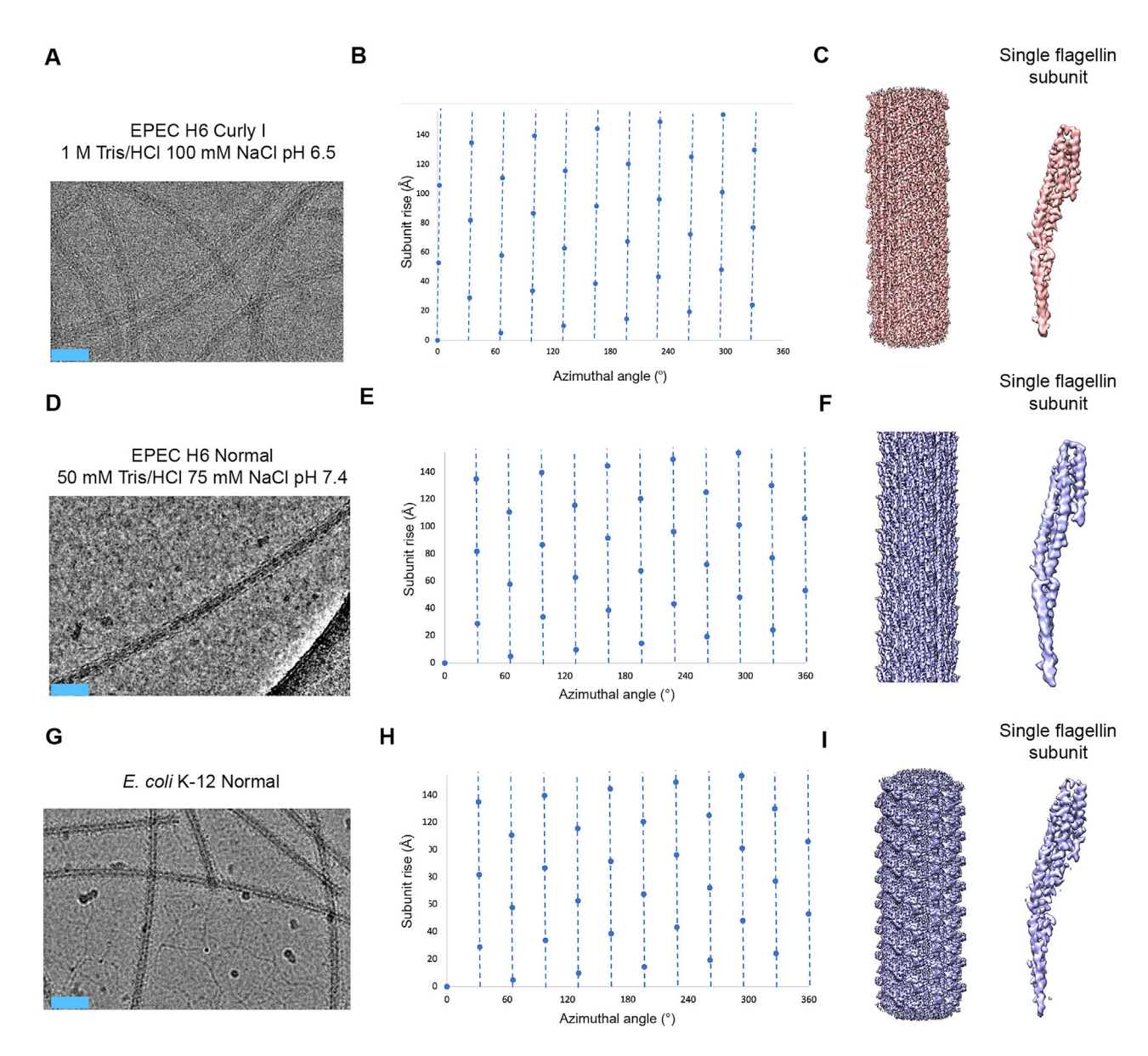


Figure S1. Cryo-EM helical reconstructions of EPEC H6 and E. coli K-12 bacterial flagellar filaments, related to Figure 1

(A) Micrograph of EPEC H6 flagellar filaments. Scale bar is $\sim\!\!50$ nm.

(B) Helical net created from the final monomeric symmetry parameters of axial rise of 4.81 Å and helical twist of 65.54° . We use the convention that the surface has been unrolled, and we are looking from the outside. The blue dashed lines represent the 11 protofilaments, which have a tilt of $+0.94^\circ/52.9$ Å, where $52.9 = 11 \times 4.81$. This tilt is a twist of 2π radians/ $2.0 \, \mu m$, or $3.1 \, \mu m^{-1}$, but would ignore any contribution from curvature, which would not exist for strict helical symmetry. (C) Density map from the monomeric symmetry helical reconstruction. Side and top views of the filament are shown on the left. A density map of a single flagellin subunit is shown on the right.

- (D) Electron micrograph of EPEC H6 flagellar filaments. Scale bar is $\sim\!50$ nm.
- (E) Helical net of from the final symmetry parameters of 4.82 Å axial rise and 65.403° helical twist, which is $-0.567^{\circ}/53.0$ Å or $-1.9~\mu m^{-1}$.
- (F) Density map from the helical reconstruction of the EPEC H6 flagellar filament in the normal waveform. Side and top views of the filament are shown on the left. A density map of a single flagellin subunit is shown on the right.
- (G) Cryo-EM of *E. coli* K-12 flagellar filaments. Scale bar is ~50 nm.
- (H) Helical net for the E. coli K-12 flagellar filament. The axial rise is 4.83 Å, and the twist is 65.406°, which is -0.534°/53.1 Å or -1.8 μm⁻¹.
- (I) Density map of the E. coli K-12 monomeric symmetry helical reconstruction. Side and top views of the filament are shown on the left. A density map of a single flagellin subunit is shown on the right.



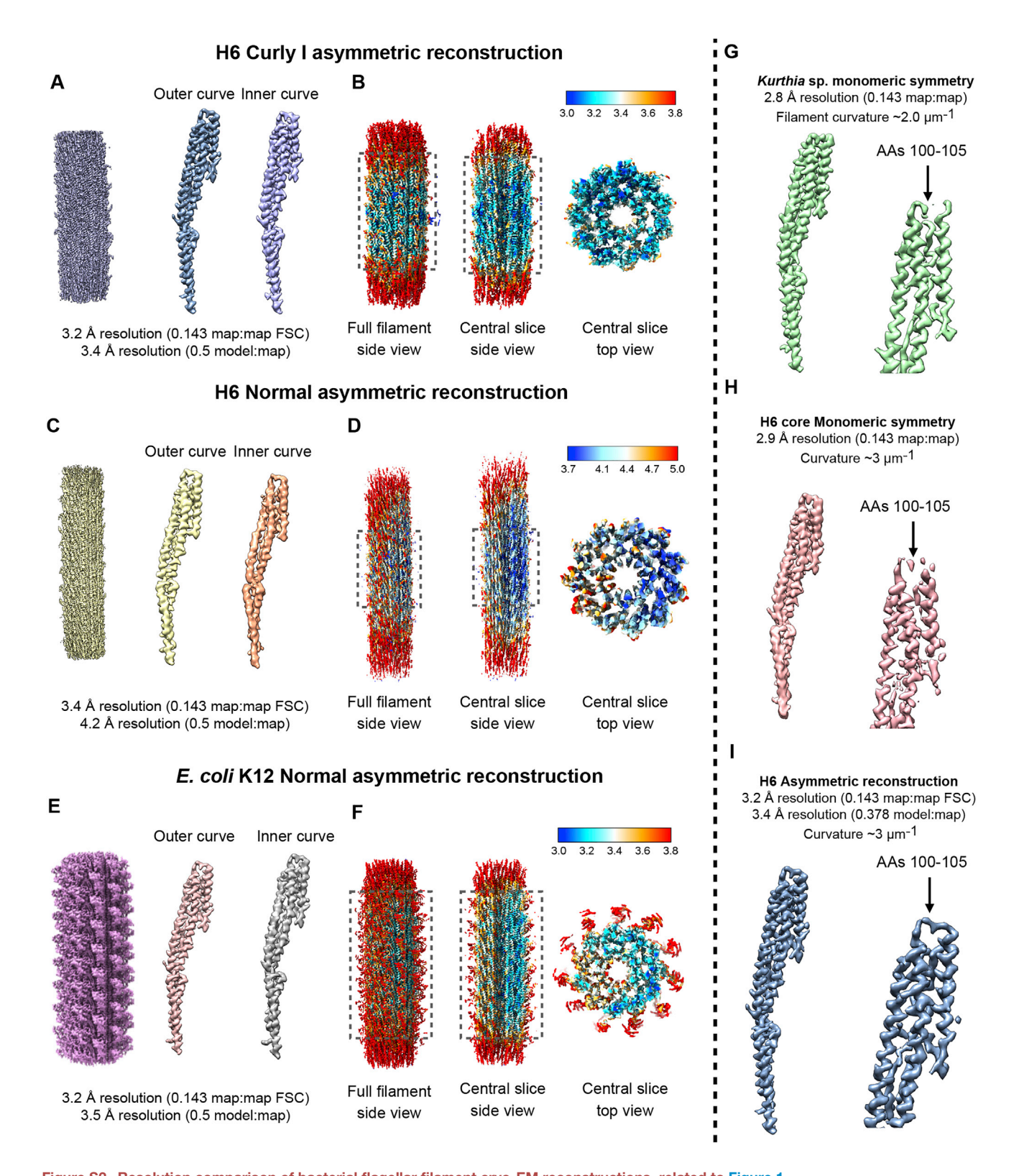


Figure S2. Resolution comparison of bacterial flagellar filament cryo-EM reconstructions, related to Figure 1

(A) Density map for the EPEC H6 curly I asymmetric reconstruction. The left map is the entire flagellar filament reconstruction. The right maps show inner and outer curve flagellin subunit densities.





(B) Local resolution estimate for the EPEC H6 curly I reconstruction. The 33-subunit curly I model was built into the middle section of the map with the highest resolution density (estimated \sim 3.2–3.4 Å). The dashed box approximately corresponds to the region used for model building.

⁽C) Filament and subunit density maps for the EPEC H6 normal asymmetric reconstruction.

⁽D) Local resolution estimate for the EPEC H6 normal asymmetric reconstruction. The dashed box approximately corresponds to the region used for model building.

⁽E) Filament and subunit density maps for the $\it E.~coli$ K-12 normal flagellar filament asymmetric reconstruction.

⁽F) Local resolution estimate for the *E. coli* K-12 normal flagellar filament asymmetric reconstruction. The lowest resolution density (red) was the beginning of the K-12 outer domain D2 and was not used in this study. The dashed box approximately corresponds to the region used for model building.

⁽G) The density map for a core (D0/D1 domain) of single Kurthia flagellin subunit. The left image shows the full core domains of the flagellin, and the right shows a close up of domain D1 density at high threshold. Broken density in domain D1 is indicated by the arrows.

⁽H) Density map for flagellin core from the H6 helical reconstruction. The full domain D0/D1 core is shown on left. On the right is an image showing the broken density in domain D1 at high threshold.

⁽I) Density map for flagellin core from the EPEC H6 asymmetric reconstruction. The left image shows the full D0/D1 core density. The right image shows a close up of domain D1 at high threshold. The density in the loop region (aas 100–106) appears quite good and not broken in contrast to the helical reconstructions.





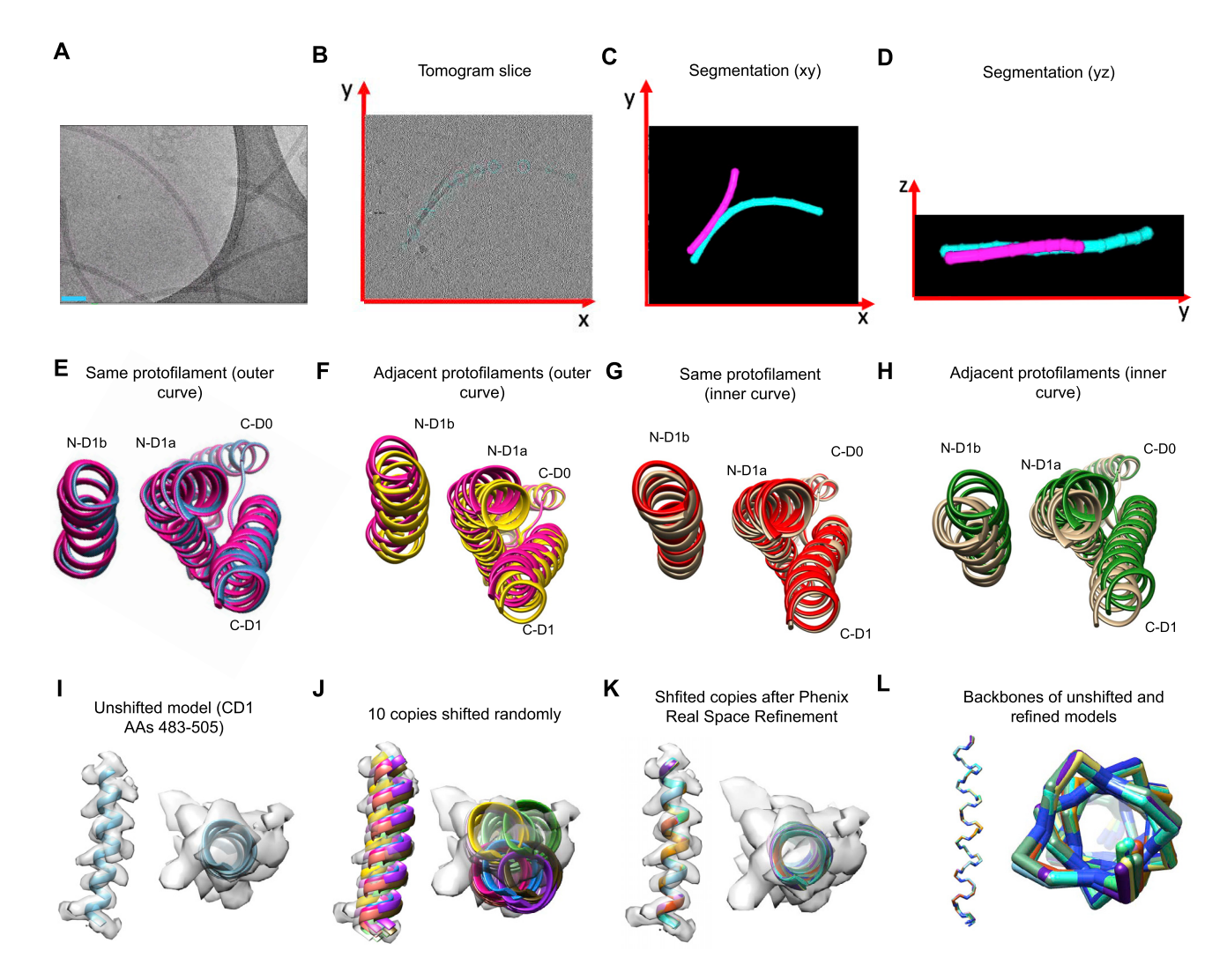


Figure S3. Cryo-electron tomography and modeling controls for bacterial flagellar filaments, related to Figures 2 and 3

- (A) Electron micrograph of wild-type *C. jejuni* flagellar filaments. The scale bar is \sim 50 nm.
- (B) Tomogram slice of C. jejuni flagellar filaments.
- (C) Segmentation of the flagellar filaments showing them in the x and y dimensions.
- (D) Segmentation of the flagellar filaments in the y and z dimensions.
- (E) Alignment of two curly I subunits from the same outer curve protofilament by domain D0.
- (F) Alignment of two curly I subunits from adjacent outer curve protofilaments by domain D0. The pink subunit is the same in both (A) and (B).
- (G) Alignment of two curly I subunits from the same inner curve protofilament by domain D0.
- (H) Alignment of two curly I subunits from adjacent inner curve protofilaments by domain D0.
- (I) Unshifted model (light blue) fit into its density map (light gray). The right image is a top view.
- (J) The randomly shifted models are shown here in different colors prior to refinement in Phenix.
- (K) Shifted models after refinement to the density map. After refinement in Phenix, the models all fit the density map quite nicely.
- (L) Backbones of the 10 refined models as well as the unshifted one.





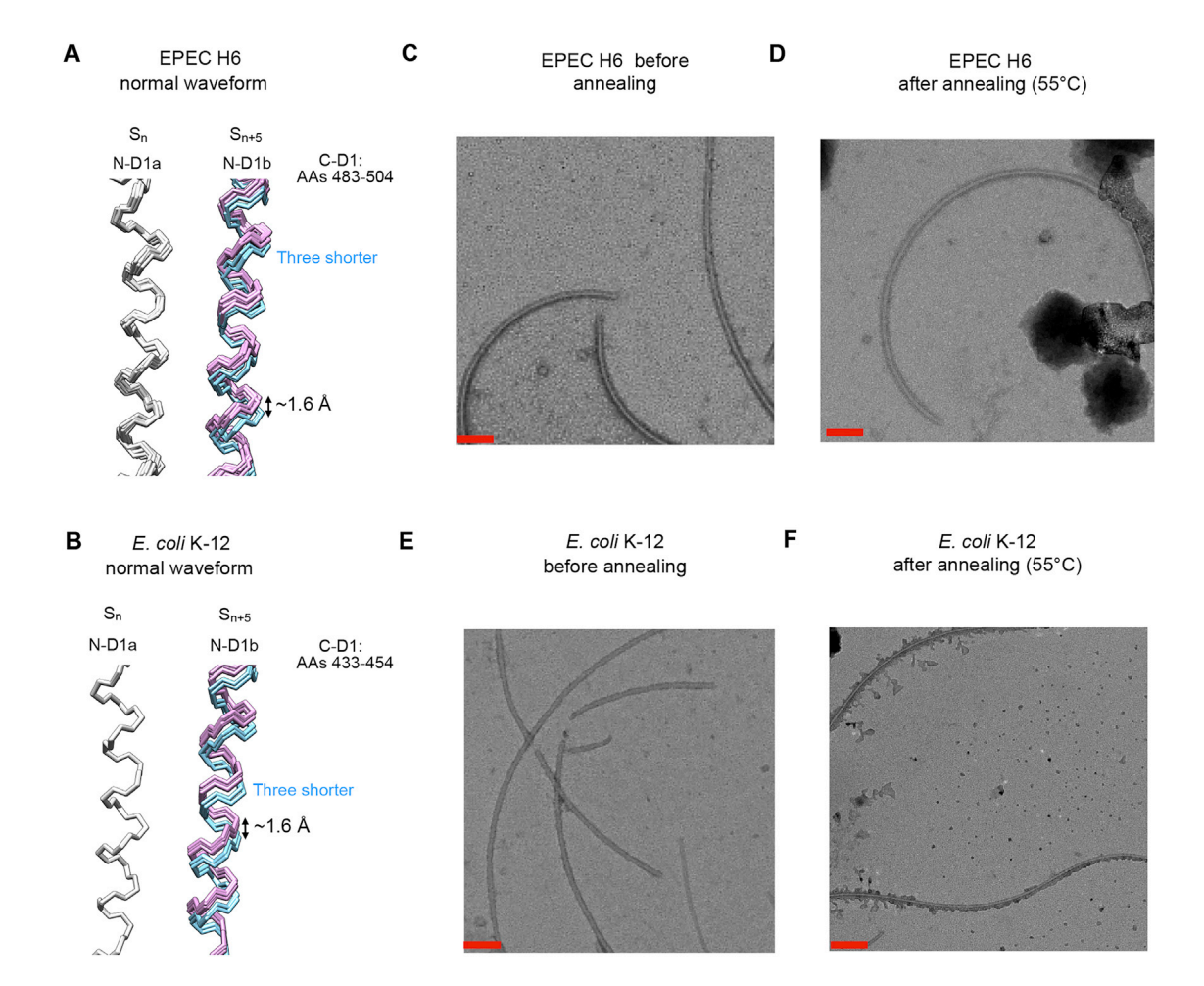


Figure S4. Comparison between EPEC H6 and *E. coli* K-12 normal-waveform 5-start interfaces and annealing experiments of supercoiled flagellar filaments, related to Figure 4

(A) 5-start interface between N-D1 domains of subunit, S_{n_i} and adjacent subunit S_{n+5} for the EPEC H6 normal flagellar filament structure. Shorter protofilaments are colored blue, and longer ones are colored pink. The \sim 1.6 Å shearing between the shortest and longest protofilament is indicated. (B) 5-start interface between N-D1 domains of subunit, S_{n_i} , and adjacent subunit S_{n+5} for the *E. coli* K-12 normal flagellar filament structure. Shorter protofilaments are colored blue, and longer ones are colored pink. The \sim 1.6 Å shearing between the shortest and longest protofilament is indicated. (C–F) In all images, the scale bars are \sim 50 nm. (C) Negative-stain TEM of EPEC H6 flagellar filaments at room temperature in PBS (pH 7.2). Filaments were stained with phosphotungstic acid (PTA) (pH 7.0). (D) Negative-stain TEM of EPEC H6 flagellar filaments after the annealing experiment. A 100- μ L aliquot of the filaments

was heated to 55°C for 30 min and then allowed to cool down to room temperature, where they remained for more than an hour. (E) Negative-stain TEM of E. coli

K-12 flagellar filaments prior to the annealing experiment. (F) Negative-stain TEM of E. coli K-12 flagellar filaments after the annealing experiment.





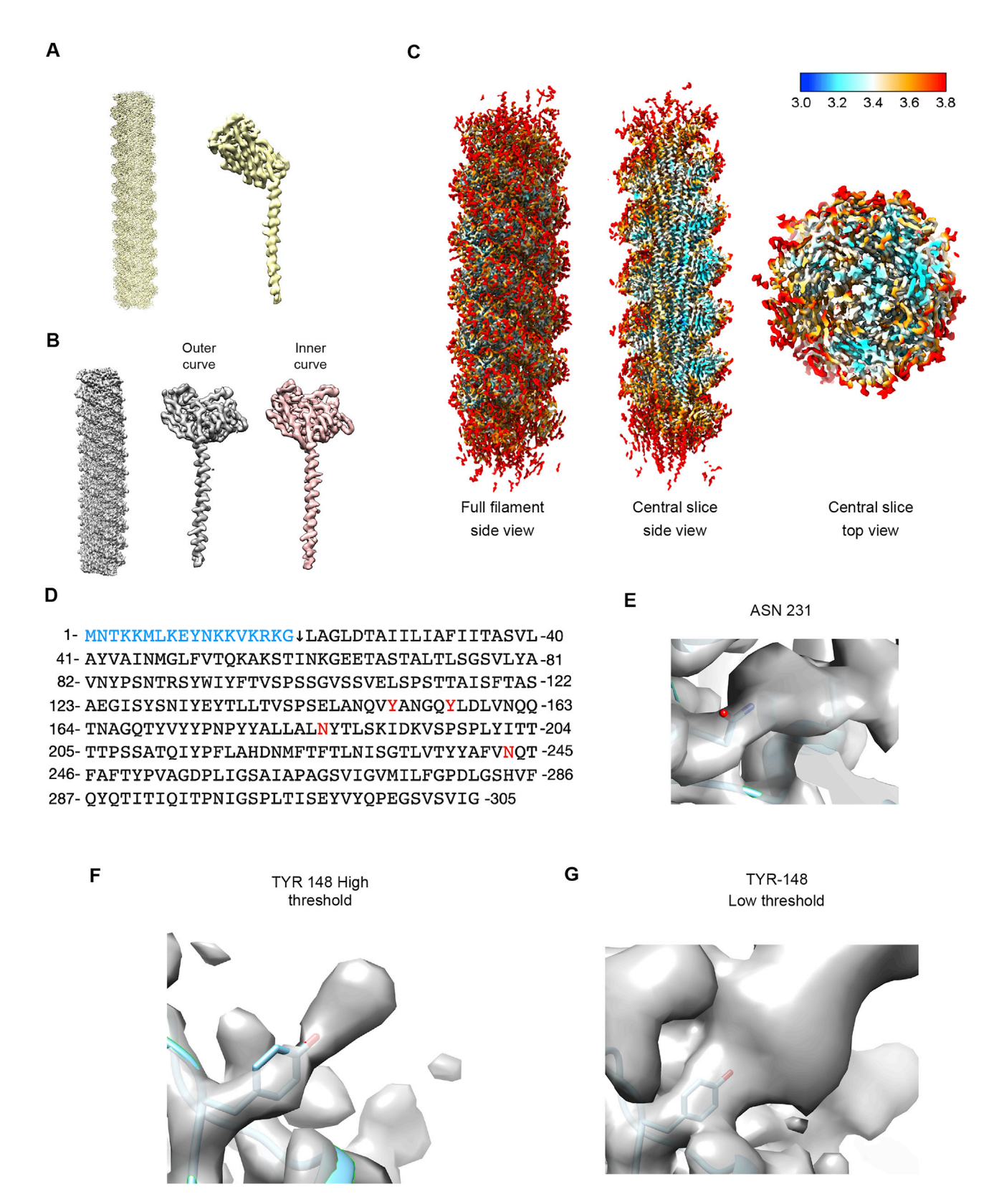






Figure S5. Density map details of the S. islandicus REY15A archaeal flagellar filament, related to Figure 5

(A) Filament and subunit density maps of the REY15A AFF helical reconstruction.

(B) Filament and subunit density maps for the REY15A asymmetric reconstruction.

(C) Local resolution estimate for the REY15A asymmetric reconstruction. The dashed box approximately corresponds to the region used for model building.

(D) Sequence of the S. islandicus REY15A archaeal flagellin. The N-terminal sequence removed in processing is shown in blue. Residues that appear glycosylated in the density map are colored red.

(E) Glycosylation of asparagine 231. The residue is shown with its large glycan density.

(F and G) Evidence of tyrosine glycosylation in the REY15A flagellar filament. (F) shows tyrosine 148 and its corresponding density at high threshold. (G) shows tyrosine 148 and its corresponding density at low threshold.



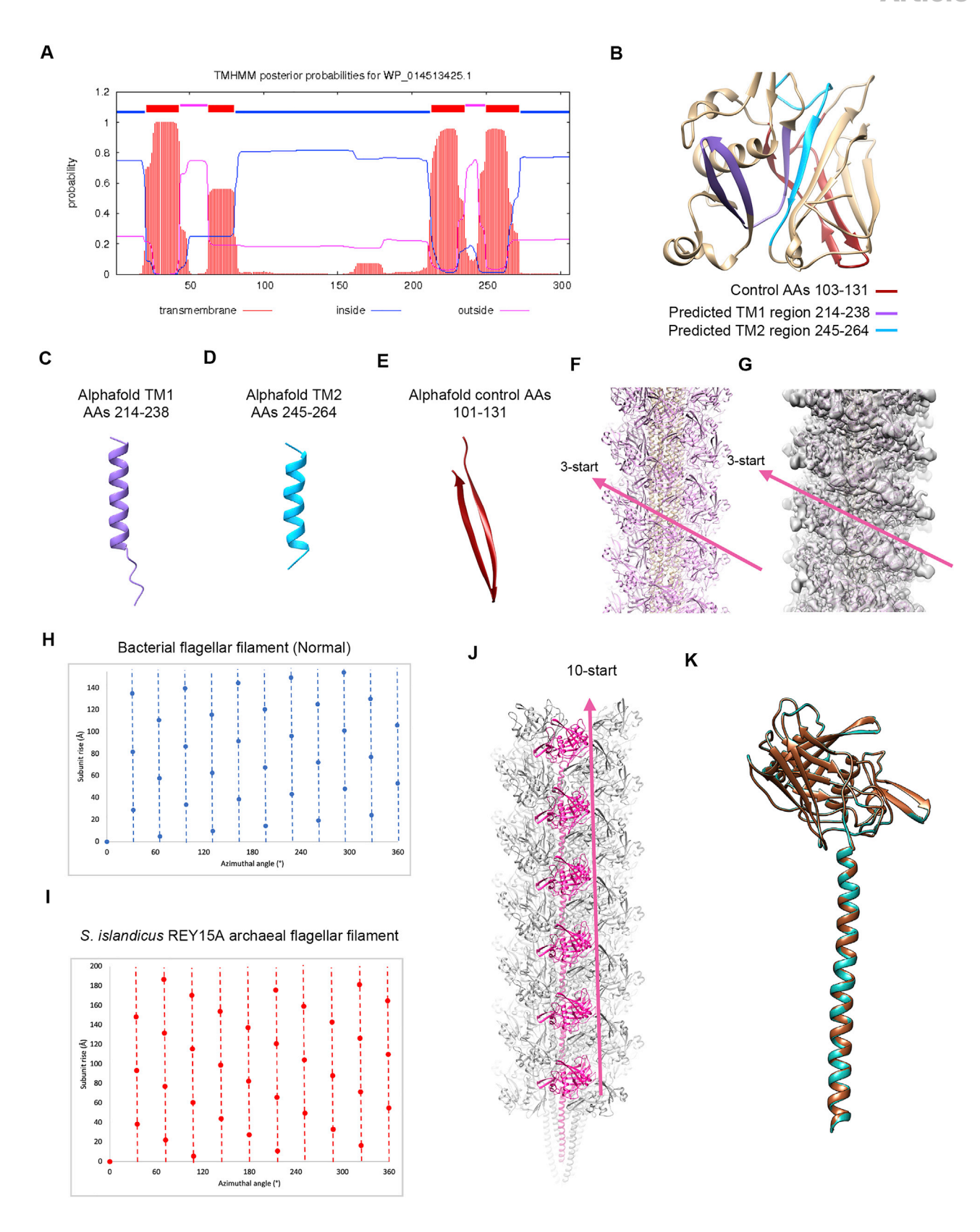






Figure S6. Sequence prediction of REY15A flagellin and the identification of archaeal flagellar protofilaments, related to Figures 5 and 6 (A) TMHMM prediction of transmembrane helices in the REY15A archaeal flagellin.

(B) Model of the REY15A C-terminal outer domain. The model was initially generated using AlphaFold prior to refinement. The regions in the model are colored according to the key at the top.

(C) AlphaFold prediction of amino acids 214–238 (purple). It should be noted that the extended loop at one of the ends of the AAs 214–238 prediction is close to being α -helical.

- (D) AlphaFold prediction of amino acids 245–264 (cyan).
- (E) The AlphaFold predicted β -hairpin for control region of AAs 101–131 (dark red). This region is not predicted to be a transmembrane helix by TMHMM and is a β -hairpin in the filament model.
- (F) Surface of the REY15A archaeal flagellar filament atomic model with the N-terminal core domains colored tan and the C-terminal outer domains colored pink. The 3-start helix formed by one set of these outer domain interactions is marked with the pink arrow.
- (G) The same view from (F) but with the density map (gray) shown as well. The extensive glycan densities make the 3-start helix even more pronounced.
- (H) Helical net of the EPEC H6 normal waveform. The 11-start protofilaments are indicated by the blue dashed lines.
- (I) Helical net of the S. islandicus REY15A archaeal flagellar filament. The 10-start protofilaments are indicated by the red dashed lines.
- (J) Depiction of the 10-start helix of the REY15A archaeal flagellar filament.
- (K) Alignment of two REY15A archaeal flagellins from the same protofilament.



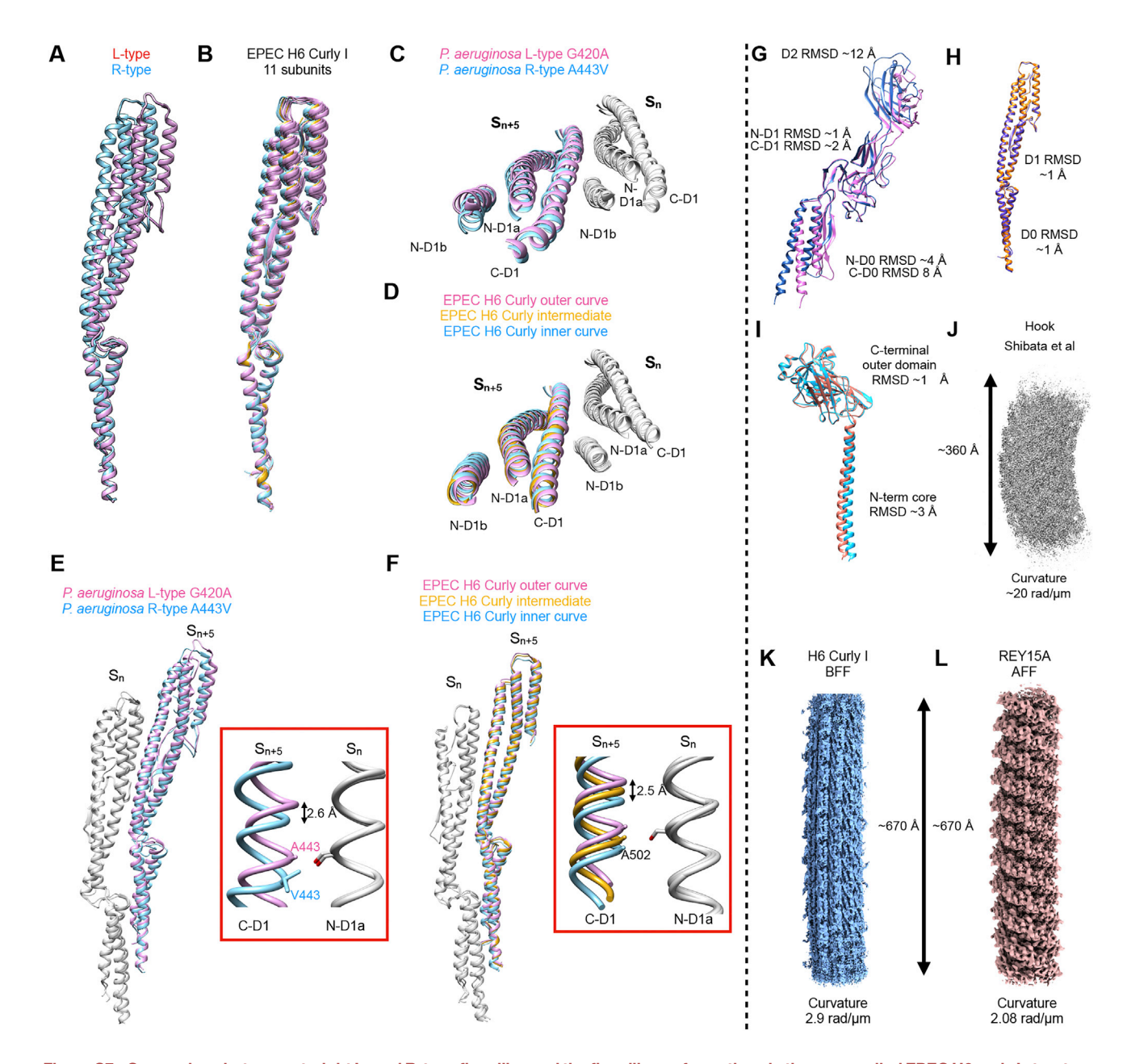


Figure S7. Comparison between straight L- and R-type flagellins and the flagellin conformations in the supercoiled EPEC H6 curly I structure, related to Figure 7

- (A) Alignment of the P. aeruginosa L-type (pink) and R-type (blue) flagellins by domain D0.
- (B) Alignment of the 11 EPEC H6 curly I subunits by domain D0.
- (C) Alignment of the L-type (pink) and R-type (blue) 5-start interfaces by subunit S_n.
- (D) Alignment of the curly I outer curve (pink), inner curve (blue), and intermediate 5-start interfaces by subunit S_n .
- (E) Alignment of the 5-start interface between L-type and R-type structures from P. aeruginosa. The two interfaces have been aligned by the subunit S_n . The left image shows the entire flagellins in the alignment. The right image shows the interface of C-D1 from subunit S_{n+5} and N-D1a from subunit S_n .
- (F) Alignment of the outer curve (pink), intermediate (gold), and inner curve (blue) 5-start interfaces in the H6 curly I model.
- (G) Alignment of inner (blue) and outer (pink) curve subunits of the supercoiled flagellar hook from Shibata et al. (2019). The subunits were aligned across the entire protein sequence.
- (H) Alignment of inner curve (orange) and outer curve (purple) EPEC H6 curly I BFF subunits. The alignment was across the entire sequence of domains D0 and D1.
- (l) Alignment of inner (orange) and outer (cyan) curve subunits of the REY15A AFF. The alignment was made using the entire protein sequence.
- (J) Density map of the supercoiled flagellar hook from Shibata et al. (2019), with the approximate curvature indicated. The curvature was estimated from Figure S1 in Shibata et al. (2019) with the pitch approximately 150 nm and the diameter approximately 50 nm.
- (K) Density map of the EPEC H6 curly I bacterial flagellar filament. Curvature is given in Table S3.
- (L) Density map of the REY15A archaeal flagellar filament. Curvature is given in Table S3.